

# When are Post-hoc Conceptual Explanations Identifiable?

Tobias Leemann<sup>1\*</sup>, Michael Kirchhof<sup>1\*</sup>, Yao Rong<sup>1</sup>, Enkelejda Kasneci<sup>2</sup>, Gjergji Kasneci<sup>1</sup>

<sup>1</sup>University of Tübingen, Germany, <sup>2</sup>Technical University of Munich, Germany

{tobias.leemann, michael.kirchhof, yao.rong, gjergji.kasneci}@uni-tuebingen.de,  
enkelejda.kasneci@tum.de}

## Abstract

Interest in understanding and factorizing learned embedding spaces through conceptual explanations is steadily growing. When no human concept labels are available, concept discovery methods search trained embedding spaces for interpretable concepts like object shape or color that can be used to provide post-hoc explanations for decisions. Unlike previous work, we argue that concept discovery should be identifiable, meaning that a number of known concepts can be provably recovered to guarantee reliability of the explanations. As a starting point, we explicitly make the connection between concept discovery and classical methods like Principal Component Analysis and Independent Component Analysis by showing that they can recover independent concepts with non-Gaussian distributions. For dependent concepts, we propose two novel approaches that exploit functional compositionality properties of image-generating processes. Our provably identifiable concept discovery methods substantially outperform competitors on a battery of experiments including hundreds of trained models and dependent concepts, where they exhibit up to 29 % better alignment with the ground truth. Our results provide a rigorous foundation for reliable concept discovery without human labels.

## 1 Introduction

Modern computer vision systems represent and reason about images in embedding spaces. These are either constructed implicitly in higher-level layers of large models or explicitly through generative models such as Variational Autoencoders [31] or Diffusion Models [20, 48]. To unveil why an image is considered similar to a certain class, interest in understanding these embeddings is increasing. Conceptual explanations [1, 12, 26, 29, 37, 56] are a popular explainable AI (XAI) technique for this purpose. They scrutinize a given encoder by decomposing its embedding

space into interpretable concepts post-hoc, i.e., after training. Subsequently, these concepts form the bases of popular post-hoc explanations such as TCAV [29] or allow high-level interventions [32]. Fig. 1 outlines a real-world example. A misclassification made by a pretrained model shipped with the `pytorch` library [40] is to be explained. In the given example, the conceptual explanation allows identification of a spurious correlation, that the model has picked up: Most jack-o-lanterns are found in combination with dark backgrounds, which causes it to mistake the traffic light at night for a jack-o-lantern.

Constructing such explanations is non-trivial. The key ingredient to all conceptual explanation techniques is a set of interpretable concepts, which is notoriously hard to specify [34]. It is frequently defined through human annotations [12, 29, 32] on individual samples of the dataset that can be prohibitively expensive [27]. Furthermore, it is usually unknown which concepts will be leveraged by a machine learning model without a model at hand. Therefore, we consider fully unsupervised concept discovery [14, 56], where the concepts are automatically discovered in the data. Concepts are frequently modeled as directions in a given embedding space [14, 29, 56], that have to be discovered without supervision. These embedding spaces can be highly distorted, making it hard to correctly separate the influences of individual concepts. However, this is essential to make the right inferences in practice (see Fig. 1d).

While many methods have been empirically shown to work well, a rigorous theoretical analysis of the conditions under which concept discovery is possible is still lacking in previous works. We propose to consider concept discovery methods that are *identifiable*. This means when a known number of *ground truth components* generated the data, the concept discovery method provably yields concepts that correspond to the individual ground truth components and can correctly represent an input in the concept space. This is a crucial requirement: If a method is even incapable of recovering known components, there is no indication for why it should be reliable in practice. In this work, we are the first to investigate identifiability results in the context of post-hoc con-

\*Equal contribution

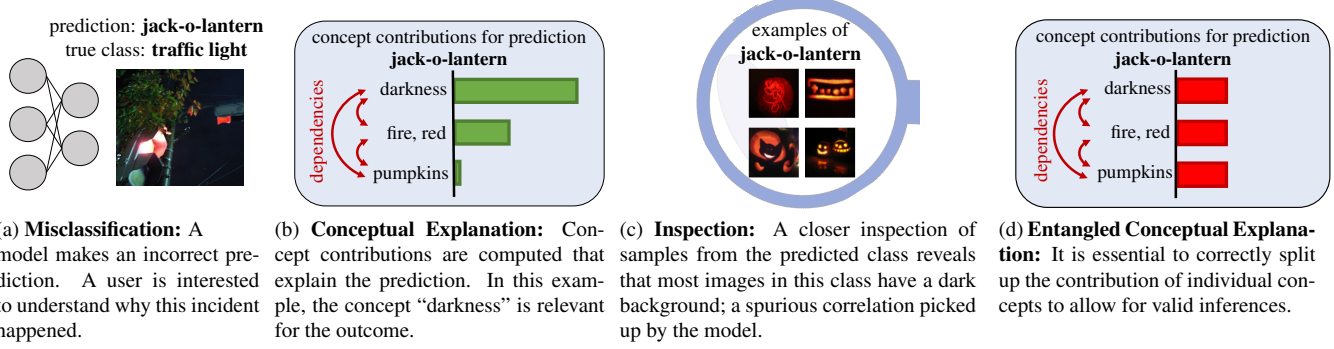


Figure 1. Schematic use-case of conceptual explanations: A misclassification of an image classifier is explained. The example is based on a real explanation for a ResNet50 model. Details and the original explanation are provided in App. C.8.

cept discovery.

First, we find that identifiability results from Principal Component Analysis (PCA) and Independent Component Analysis (ICA) literature [11, 22, 25] can be transferred to the conceptual explanation setup. We establish that they cover the case of independent ground truth components with non-Gaussian distributions. This is insufficient for two reasons: (1) In practice, concepts such as height and weight [51] or wing and head colors of birds often follow complex dependency patterns. (2) Popular generative models [31, 48] frequently work with an embedding space with a Gaussian distribution.

As a second contribution, we seek to fill this void by providing an identifiable concept discovery approach that can handle dependent and Gaussian ground truth components. We can show that this is possible through taking the nature of the image-generating process into consideration. Specifically, we propose utilizing *visual compositionality properties*. These are based on the observation that tiny changes in the components frequently affect input images in orthogonal or even disjoint ways. These properties of image-generating processes also leave a “trace” in the encoders learned from a set of data samples. This insightful finding permits to construct two novel post-hoc concept discovery methods based on the *disjoint* or *independent mechanisms* criterion. We prove strong identifiability guarantees for recovering components, even if they are dependent.

In summary, our work advances current literature in multiple ways: (1) We present first identifiability results for post-hoc conceptual explanations. We find that results from ICA can be transferred under independent ground truth components. (2) For the more intricate setting of dependent components, we derive the *disjoint mechanism analysis (DMA)* and the less constrained *independent mechanism analysis (IMA)* criterion. We prove that they recover even dependent original components up to permutation and scale. (3)

We construct DMA and IMA-based concept discovery algorithms for encoder embedding spaces with the same theoretical identifiability guarantees. (4) We test them (i) on embeddings of several autoencoder models learned from correlated data, (ii) with multiple and strong correlations, (iii) on discriminative encoders, and (iv) on the real-world CUB-200-2011 dataset [53]. Our approaches maintain superior performance amidst increasingly severe challenges.

## 2 Related Work

Works on the analysis and interpretation of embedding spaces touch a variety of subfields of machine learning.

**Concept discovery for explainable AI.** Conceptual explanations [1, 10, 14, 29, 32, 56] have gained popularity within the XAI community. They aim to explain a trained machine learning model post-hoc in terms of human-friendly, high-level concept directions [29]. These concepts are found via supervised [26, 30, 32] or unsupervised approaches [1, 42, 56], such as clustering of embeddings [14]. However, their results are not always meaningful [34, 56]. Therefore, we suggest approaches with identifiability guarantees. We provide initial identifiability results and a novel approach which can be used for unsupervised concept discovery under correlated components.

**Independent Component Analysis (ICA).** Independent Component Analysis [11, 22, 23] or blind source separation (BSS) view  $g(z)$  as a mixture to undo and rely on traces that the distributions over  $z$  leave in the mixture. In this work, we show that an identifiability result from ICA can be transferred to the conceptual explanation setup, but recovery is only possible under independent underlying components of which all but one are non-Gaussian. This result is not applicable to naturally correlated processes, which is why we design a novel method for this case.

**Disentanglement Learning.** Concurrently, literature in on disentanglement learning is concerned with finding a data-generating mechanism  $g(z)$  and a latent representation  $z$  for a dataset, such that each of the original components (also known as factors of variation) is mapped to one (controllable) unit direction in  $z$  [4]. An alternative definition relies on group theory [19] where certain group operations (symmetries) should be reflected in the learned representation [39, 55]. Most works in the domain enhance VAEs [31] with additional loss terms [7, 8, 19, 30]. Despite recent progress it is not always possible to construct disentangled embedding spaces from scratch: [35] have shown that the problem is inherently unidentifiable without additional assumptions. A more recent work by Träuble et al. [51] shows that even if just two components of a dataset are correlated, current disentanglement learning methods fail. In this work, we focus on post-hoc explanations of embedding spaces of given models, which are usually entangled.

**Identifiability results.** A strain of works have considered identifiability in disentanglement learning. It has been previously shown that unsupervised disentanglement, without further condition, is impossible [23, 35]. Hence, recent works aim to understand the conditions sufficient for identifiability. One strain of work relies on additional supervision, i.e., access to an additional observed variable [24, 28] or to tuples of observations that differ in only a limited number of components [36]. Gresele et al. [17] and Zheng et al. [57] proved identifiable disentanglement under independently distributed components and introduce a functional condition on the data generator. We also consider functional properties but our setting is different as (1) we have access to a trained encoder only and (2) not even partial annotations or relations are available.

### 3 Analysis

In this section, we formalize post-hoc concept discovery to provide an identifiability perspective. We find that Independent Component Analysis (ICA) and Principal Component Analysis (PCA) only guarantee identifiability when the ground-truth components are stochastically independent. We then study the intricate case of dependent components and propose using *disjoint* and *independent mechanisms analysis* (DMA / IMA) along with identifiability results. All proofs are provided in the supplementary.

#### 3.1 Problem Formalization

In post-hoc concept discovery, we are given a trained encoder  $f : \mathcal{X} \rightarrow \mathcal{E}$  with embeddings  $e = f(x) \in \mathcal{E} \subset \mathbb{R}^K$  of each image  $x \in \mathcal{X}$ . We do not impose any restriction on how  $f$  was obtained; it can be a the feature extractor part

of a large classification model or a feature representation learned through autoencoding, contrastive learning [9] or related techniques. Interpretability literature seeks to understand the embedding space by factorizing it into concepts. Based on the observations that directions in the embedding space often correspond to meaningful features [2, 3, 5, 50], these concepts are frequently defined as direction vectors  $m_i$  [14, 29, 56]. Hence, the combined output of a concept discovery algorithm is a matrix  $M = [m_1, \dots, m_K]^\top \in \mathbb{R}^{K \times K}$  where each row contains a concept direction.

We seek a theoretical guarantee on when these discovered concept directions align with ground truth components that generated the data. To this end, we formalize the data-generating process as shown in Fig. 2: There are  $K$  ground-truth components with scores  $z_k, k = 1 \dots K$ , summarized  $z \in \mathcal{Z} \subset \mathbb{R}^K$ , that define an image. The term *components* always refers to the ground truth as opposed to the *concepts*, which denote the discovered directions. A data-generating process  $g : \mathcal{Z} \rightarrow \mathcal{X}$  generates images  $x = g(z) \in \mathcal{X} \subset \mathbb{R}^L$ ,  $L \gg K$ . A powerful algorithm should be able to recover the original components. That is, there should be a one-to-one mapping between entries of  $Me$  and the entries in  $z$ , up to the arbitrary scale and order of the entries. We say that a concept discovery algorithm *identifies* the true components if it is guaranteed to output directions  $M$  that satisfy  $Me = Mf(g(z)) = PSz \forall z \in \mathcal{Z}$ , where  $P \in \mathbb{R}^{K \times K}$  is a permutation matrix that has one 1 per row and column and is 0 otherwise, and  $S \in \mathbb{R}^{K \times K}$  is an invertible diagonal scaling matrix.

To make the problem solvable in the first place, concept directions must exist in the embedding space of the given encoder, requiring  $e = Dz$ , where  $D \in \mathbb{R}^{K \times K}$  is full-rank. Depending on the scope of the conceptual explanation desired, it can be sufficient for the components to exist in a local region of the embedding space if the concept discovery algorithm is only applied around a region around a certain point of interest. This only changes the meaning of  $\mathcal{E}, \mathcal{X}$ , and  $\mathcal{Z}$ , but is formally equivalent.

#### 3.2 Identifiability via Independence

Initially, we turn towards classical component analysis methods. We find that they require non-correlation or stronger stochastic independence of the ground truth components.

Principal Component Analysis (PCA) [25] uses eigenvector decompositions to find orthogonal directions  $M$  that result in uncorrelated components  $Me$ . This means that PCA is only capable of identifying the original components if the ground truth components  $z$  were uncorrelated and exist as orthogonal directions in our embedding space. In our setup

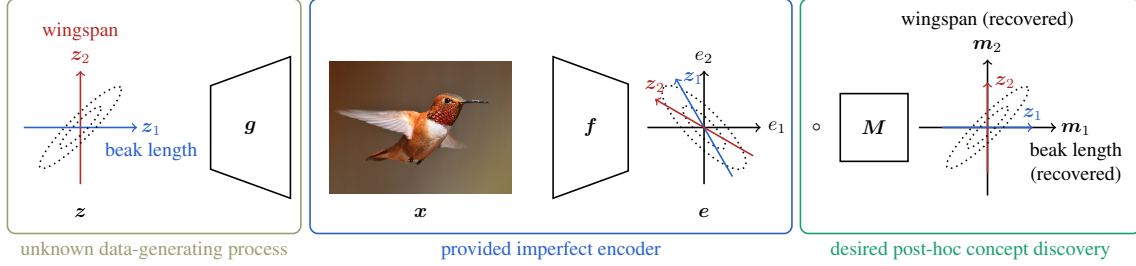


Figure 2. Overview over the concept discovery setup. We consider a process where data samples  $\mathbf{x}$  are generated from possibly correlated ground truth components  $\mathbf{z}$ , e.g., a wingspan or beak length of a bird, by an unknown process  $\mathbf{g}$  (left). The high-dimensional data is mapped to the embedding space of a given model  $\mathbf{f}$  (center). A suitable post-hoc concept discovery yields concept vectors  $\mathbf{m}_i$  that correspond to the original components (right).

and notation, this leads to the following result:

**Theorem 3.1** (PCA identifiability). *Let  $z_k, k = 1, \dots, K$ , be uncorrelated random variables with non-zero and unequal variances. Let  $\mathbf{e} = \mathbf{D}\mathbf{z}$ , where  $\mathbf{D} \in \mathbb{R}^{K \times K}$  is an orthonormal matrix. If an orthonormal post-hoc transformation  $\mathbf{M} \in \mathbb{R}^{K \times K}$  results in mutually uncorrelated components  $(z'_1, \dots, z'_K) = \mathbf{z}' = \mathbf{M}\mathbf{e}$ , then  $\mathbf{M}\mathbf{e} = \mathbf{P}\mathbf{S}\mathbf{z}$ , where  $\mathbf{P} \in \mathbb{R}^{K \times K}$  is a perm. and  $\mathbf{S} \in \mathbb{R}^{K \times K}$  is a diag. matrix where  $|s_{ii}| = 1$  for  $i \in 1, \dots, K$ .<sup>1</sup>*

All proofs in this work are deferred to App. B. It is arguably a strong condition that the ground truth directions are encoded orthogonally in the embedding space. Independent Component Analysis (ICA) overcomes this limitation [11] and allows for arbitrary directions, but requires stochastically independent components instead of the weaker non-correlation.

**Theorem 3.2** (ICA identifiability). *Let  $z_k, k = 1, \dots, K$ , be independent random variables with non-zero variances where at most one component is Gaussian. Let  $\mathbf{e} = \mathbf{D}\mathbf{z}$ , where  $\mathbf{D} \in \mathbb{R}^{K \times K}$  has full rank. If a post-hoc transformation  $\mathbf{M} \in \mathbb{R}^{N \times N}$  results in mutually independent components  $(z'_1, \dots, z'_K) = \mathbf{z}' = \mathbf{M}\mathbf{e}$ , then  $\mathbf{M}\mathbf{e} = \mathbf{P}\mathbf{S}\mathbf{z}$ , where  $\mathbf{P} \in \mathbb{R}^{K \times K}$  is a perm. and  $\mathbf{S} \in \mathbb{R}^{K \times K}$  is a diag. matrix.*

This result shows that stochastic independence of the ground truth components leaves a strong trace in the embeddings that can be leveraged. Algorithms like `fastICA` [21] can find the concept directions  $\mathbf{M}$  by searching for independence [11]. We conclude that ICA is suited for post-hoc concept discovery under independent components.

In summary, we have transferred two results from the component analysis literature to the setup of post-hoc conceptual explanations. However these results do not allow to

<sup>1</sup>To simplify notation,  $\mathbf{P}$  and  $\mathbf{S}$  mean any permutation and scale matrices. They do not have to be equal between the theorems.

Dependency	Marginal Dist.	Transform	Criterion
uncorr.	uneq. variances	orthogonal	non-correlation (PCA)
independent	non-Gaussian	invertible	independence (ICA)
arbitrary	arbitrary	invertible	disj. mechanisms (DMA)
arbitrary	arbitrary	invertible	indep. mechanisms (IMA)

Table 1. PCA and ICA provably identify concepts via their distributions. DMA and IMA utilize functional properties.

recover components that are correlated or follow a Gaussian distribution. This limits their applicability in practice where concepts often appear pairwise (e.g., darkness and jack-o-lanterns, cf. Fig. 1). We will bridge this gap in the remainder of this paper by introducing two new identifiable discovery methods based on functional properties of the generation process that we term *disjoint* and *independent* mechanisms. A summary of identifiability results is provided in Table 1.

### 3.3 Identifiability via Disjoint Mechanisms

Instead of placing independence assumptions on  $\mathbf{z}$ , we propose a concept discovery algorithm that makes use of natural properties of the generative process  $\mathbf{g}$ . In particular, generative processes in vision are often compositional [38]: Different groups of pixels in an image, like a bird’s wings, legs, and head, are each controlled by different components. Effects of tiny changes in components are visible in the Jacobian  $\mathbf{J}_g$ , where each row points to the pixels affected. Thus, a compositional process will follow the *disjoint mechanisms* principle.

**Definition 3.1** (Disjoint mechanisms).  *$\mathbf{g}$  is said to generate  $\mathbf{x}$  from its components  $\mathbf{z}$  via disjoint mechanisms if the Jacobian  $\mathbf{J}_g(\mathbf{z}) \in \mathbb{R}^{L \times K}$  exists and is a block matrix  $\forall \mathbf{z} \in \mathcal{Z}$ . That is, the columns of  $\mathbf{J}_g(\mathbf{z})$  are non-zero at disjoint rows, i.e.  $|\mathbf{J}_g(\mathbf{z})|^T |\mathbf{J}_g(\mathbf{z})| = \mathbf{S}(\mathbf{z})$ , where  $\mathbf{S} \in \mathbb{R}^{K \times K}$  is a diagonal matrix that may be different for each  $\mathbf{z}$  and  $|\cdot|$  takes the element-wise absolute value.*

Note that this definition does not globally constrain the location of affected pixels such that components may be altered, different, but disjoint pixels in each image. In real concept discovery, we do not have access to the generative process  $g$  but can only access the encoder  $f$ . However, an encoder corresponding to  $g$  will not be arbitrary and its Jacobian  $J_f \in \mathbb{R}^{K \times L}$  have a distinct form in practice: First, to maintain the component information the composition  $f \circ g$  will be of the form  $f(g(z)) = Dz$ , with a yet unknown matrix  $D \in \mathbb{R}^{K \times K}$ . Furthermore, we expect encoders to be rather lazy, meaning they only perform the changes to invert the data generation process but are almost invariant to input deviations not due to changes in the components. Technically, the changes effected by the components form the linear span( $J_g(z)$ ), whereas entirely external changes are given in its orthogonal complement  $\text{span}(J_g(z))^\perp$ . Thus, for  $v \in \text{span}(J_g(z))^\perp \subset \mathbb{R}^L$  the encoder should not react to these, i.e.,  $J_f(z)v = 0 \Leftrightarrow v \in \ker(J_f(z))$ .

**Definition 3.2** (Faithful encoder).  *$f$  is a faithful encoder for the generative process  $g$  if the ground truth components remain recoverable, i.e.,  $f(g(z)) = Dz$ , for some  $D \in \mathbb{R}^{K \times K}$  with full rank. Furthermore,  $f$  is lazy and invariant to changes in  $x$  which cannot be explained by the ground truth components, requiring  $J_f(g(z))$  and  $J_g(z)$  to exist and  $\text{span}(J_g(z))^\perp \subseteq \ker(J_f(z))$ ,  $\forall z \in \mathcal{Z}$ .*

Having defined what realistic encoders look like, we find, there is a distinct property which can be leveraged to discover the directions in  $M$  among faithful encoders: It is necessary to find a decoder  $Mf$  whose Jacobian  $MJ_f$  will have disjoint rows. Intuitively, this requires searching for components whose gradients affect disjoint image regions.

**Theorem 3.3** (Identifiability under DMA). *Let  $g$  have disjoint mechanisms and  $f$  be a faithful encoder to  $g$ . If a full-rank post-hoc transformation  $M \in \mathbb{R}^{K \times K}$  results in disjoint rows in the Jacobian  $MJ_f(g(z))$ , i.e.,  $|MJ_f(g(z))|MJ_f(g(z))^\top$  is invertible and diagonal for some  $z \in \mathcal{Z}$ , then  $Me = PSz$ , where  $P \in \mathbb{R}^{K \times K}$  is a permutation and  $S \in \mathbb{R}^{K \times K}$  is a scaling matrix.*

This theorem does not impose any restrictions on the distribution  $z$ , making it applicable to realistic concept discovery scenarios through leveraging the nature of the generative process. The proof of this algorithm in App. B.5 also yields an analytical solution. We will use it to verify conditions in a controlled experiment in Sec. 4.1. We have thus identified the *DMA criterion* that allows to discover the component directions: The rows of  $MJ_f$  need to point to disjoint image regions. We can formulate this as a loss function and optimize for  $M$  via off-the-shelf gradient descent:

$$\mathcal{L}(M) = \mathbb{E}_x \|\text{arn}[MJ_f(x)] \text{arn}[MJ_f(x)]^\top - I\|_F^2. \quad (1)$$

The expectation is taken over a collection of real data samples  $x$ . The `arn`-operator (`absolute values, row normalization`) takes the element-wise absolute value and subsequently normalizes the rows. This does not constrain the norms of the Jacobian's rows but only enforces disjointness.

### 3.4 Concept Discovery via Independent Mechanisms

We can perform an analogous derivation for a class of generating processes that is more general. Grounded by causal principles instead of compositionality, the independent mechanisms property has been argued to define a class of natural generators [17].

**Definition 3.3** (Independent mechanisms (IMA)).  *$g$  is said to generate  $x$  from its components  $z$  via independent mechanisms if the Jacobian  $J_g(z)$  of  $g$  exists and its columns (one per component) are orthogonal  $\forall z \in \mathcal{Z}$ , i.e.,  $J_g^\top(z)J_g(z) = S(z)$ , where  $S \in \mathbb{R}^{K \times K}$  is a diagonal matrix that may differ for each  $z$  [17].*

Gresele et al. [17] and Zheng et al. [57] used this characteristic to find disentangled data generators, but we can again transfer characteristics via faithful encoders: This time we find that searching for an  $MJ_f$  with *orthogonal* (instead of disjoint) rows permits post-hoc discovery of concepts. We refer to this property of  $MJ_f$  as the *IMA criterion*.

However, as the class of admissible processes has been increased, it is not strong enough to ensure identifiability in the most general case. This is prevented under an additional technical condition on the component magnitudes, which we refer to as *non-equal magnitude ratios* (NEMR). Intuitively, it requires that the magnitudes of the component gradients change non-uniformly between at least two points.

**Theorem 3.4** (Identifiability under IMA). *Let  $g$  adhere to IMA. Let  $f$  be a faithful encoder to  $g$ . Suppose we have obtained an  $f' = Mf$  with a full-rank  $M \in \mathbb{R}^{K \times K}$  and orthogonal rows in its Jacobian  $MJ_f(g(z)) = J_{f'}(g(z))$ , i.e.,  $J_{f'}^\top(g(z))J_{f'}(g(z))^\top = \Sigma(z)$  where  $\Sigma(z)$  is diagonal and full-rank at two points  $z \in \{z_a, z_b\}$ . If additionally  $\Sigma(z_a)\Sigma(z_b)^{-1}$  has unequal entries its diagonal (NEMR condition), then  $Me = PSz$ , where  $P \in \mathbb{R}^{K \times K}$  is a permutation and  $S \in \mathbb{R}^{K \times K}$  is a scaling matrix.*

The constructive proof in App. B.6 can also be condensed into an analytical solution. Alternatively, one can again construct a suitable optimization objective for the IMA criterion, i.e., orthogonal Jacobians. This is achieved by removing the absolute value operation from the `arn`-operator in

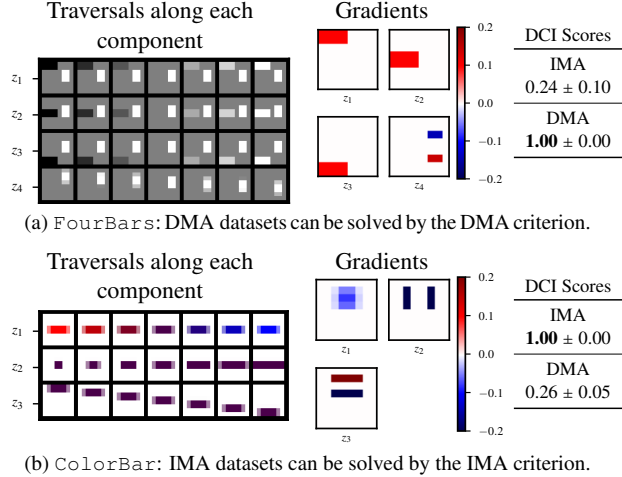


Figure 3. Experiments on two synthetic datasets: We confirm our analytic results and show that DMA (a) and IMA (b) cover realistic visual concepts such as colors and translations

Eqn. (1), so that it solely performs a row-wise normalization. In summary, we have established the novel DMA and IMA criteria that allow concept discovery under dependent concepts.

## 4 Experiments

In the following, we perform a battery of experiments of increasing complexity to compare the practical capabilities of approaches for identifiable concept discovery. We start by verifying the theoretical identifiability conditions (Sec. 4.1), then perform evaluation under increasing multi-component correlations for embedding spaces of generative and discriminative models (Sec. 4.2 to 4.4), and finally use a large-scale, discriminatively-trained ResNet50 encoder (Sec. 4.5).

We borrow the DCI metric [13] from disentanglement learning with scores in  $[0, 1]$  to measure whether each discovered component predicts precisely one ground-truth component and vice versa. Following Locatello et al. [36], we report additional metrics with similar results in App. D, along with results on additional datasets and ablations. For reproducibility, each experiment is repeated on five seeds and code is made available upon acceptance. In total, we train and analyze over 300 embedding spaces, requiring about 124 Nvidia RTX2080Ti GPU days. More implementation details are in App. C.2.

### 4.1 Confirming Identifiability

We first confirm our identifiability guarantees with the analytical solutions. To this end, we implement two realistic synthetic datasets with differentiable generators. This allows computing the closed-form of  $J_g$  and deliberately fulfilling or violating the DMA, IMA, and NEMR conditions.

FourBars consists of gray-scale images of four components: Three bars change their colors (black to white) and one bar moves vertically, showing that the image regions affected by each component may change in each image. The plot of  $J_g$  in Fig. 3a shows that each component maps to a disjoint image region. This fulfills DMA and thus also IMA. However, all factors have the same gradient magnitudes, making it impossible to find two points with NEMR. According to our theory, we expect DMA optimization to work and IMA to fail. The second dataset, ColorBar, contains a single bar that undergoes realistic changes in color, width, and its vertical position, see Fig. 3b. It conforms to IMA and NEMR but not DMA. Our proofs indicate that IMA should work and DMA fail. Completing the problem formalization in Sec. 3.1, we compute analytical faithful encoders  $f$  for these datasets distorted by a random matrix  $D$ . The solutions behave as expected: On FourBars, only the DMA criterion delivers perfectly recovered components (DCI=1) whereas only IMA succeeds on ColorBars.

### 4.2 Correlated Components

We now move to the common Shapes3D [6] dataset. It shows geometric bodies that vary in their colors, shape, orientation, size, and background totaling six components. Compared to the previous section we train real encoders. We start our analysis where disentanglement learning is no longer possible: When components are correlated. Following Träuble et al. [51], the dataset is resampled such that two components  $z_i, z_j \in [0, 1]$  follow  $z_i - z_j \sim \mathcal{N}(0, s^2)$ . Lower  $s$  results in a stronger correlation where only few pairs of component values co-occur frequently. We choose a moderate correlation of  $s = 0.4$  here and three pairs  $z_i, z_j$  that are nominal/nominal, nominal/ordinal, and ordinal/ordinal variables. We train four state-of-the-art disentanglement learning VAEs (BetaVAE [19], FactorVAE [30], BetaTCVAE [8], DipVAE [33]) from a recent study [35] and apply ICA, PCA, and our DMA and IMA discovery methods on their embedding spaces to post-hoc recover the original components. For DMA and IMA, we use the optimization-based algorithms (Eqn. 1) since they appear more robust to the noisy gradient estimates as demonstrated in App. C.1.

Sec. 4.2 shows the resulting DCI scores. In line with Träuble et al. [51], we find that the disentanglement learning

Correlated components	floor & background	orientation & background	orientation & size
<b>BetaVAE</b>	$0.497 \pm 0.03$	$0.581 \pm 0.04$	$0.491 \pm 0.05$
+PCA	$0.263 \pm 0.03$ <b>-47%</b>	$0.310 \pm 0.02$ <b>-47%</b>	$0.324 \pm 0.04$ <b>-34%</b>
+ICA	$0.574 \pm 0.04$ <b>+16%</b>	$0.540 \pm 0.08$ <b>-7%</b>	$0.577 \pm 0.04$ <b>+17%</b>
+Ours (IMA)	$0.617 \pm 0.02$ <b>+24%</b>	$0.602 \pm 0.05$ <b>+3%</b>	$0.579 \pm 0.03$ <b>+18%</b>
+Ours (DMA)	<b><math>0.641 \pm 0.03</math> <b>+29%</b></b>	<b><math>0.624 \pm 0.06</math> <b>+7%</b></b>	<b><math>0.627 \pm 0.03</math> <b>+28%</b></b>
<b>FactorVAE</b>	$0.507 \pm 0.11$	$0.502 \pm 0.08$	<b><math>0.712 \pm 0.01</math></b>
+PCA	$0.358 \pm 0.07$ <b>-29%</b>	$0.474 \pm 0.05$ <b>-5%</b>	$0.556 \pm 0.03$ <b>-22%</b>
+ICA	$0.294 \pm 0.07$ <b>-42%</b>	$0.263 \pm 0.05$ <b>-48%</b>	$0.340 \pm 0.03$ <b>-52%</b>
+Ours (IMA)	$0.551 \pm 0.04$ <b>+9%</b>	$0.498 \pm 0.03$ <b>-1%</b>	$0.595 \pm 0.05$ <b>-16%</b>
+Ours (DMA)	<b><math>0.584 \pm 0.05</math> <b>+15%</b></b>	<b><math>0.510 \pm 0.05</math> <b>+2%</b></b>	<b><math>0.556 \pm 0.04</math> <b>-22%</b></b>
<b>BetaTCVAE</b>	$0.619 \pm 0.01$	$0.613 \pm 0.04$	$0.659 \pm 0.01$
+PCA	$0.400 \pm 0.03$ <b>-35%</b>	$0.421 \pm 0.07$ <b>-31%</b>	$0.450 \pm 0.07$ <b>-32%</b>
+ICA	$0.540 \pm 0.02$ <b>-13%</b>	$0.497 \pm 0.04$ <b>-19%</b>	$0.627 \pm 0.02$ <b>-5%</b>
+Ours (IMA)	$0.623 \pm 0.02$ <b>+1%</b>	$0.652 \pm 0.03$ <b>+6%</b>	$0.638 \pm 0.04$ <b>-3%</b>
+Ours (DMA)	<b><math>0.666 \pm 0.01</math> <b>+8%</b></b>	<b><math>0.664 \pm 0.02</math> <b>+8%</b></b>	<b><math>0.748 \pm 0.03</math> <b>+14%</b></b>
<b>DipVAE</b>	$0.631 \pm 0.02$	$0.652 \pm 0.02$	$0.548 \pm 0.04$
+PCA	$0.158 \pm 0.01$ <b>-75%</b>	$0.160 \pm 0.02$ <b>-75%</b>	$0.170 \pm 0.02$ <b>-69%</b>
+ICA	$0.630 \pm 0.02$ <b>-0%</b>	$0.651 \pm 0.02$ <b>-0%</b>	$0.542 \pm 0.03$ <b>-1%</b>
+Ours (IMA)	$0.644 \pm 0.02$ <b>+2%</b>	$0.624 \pm 0.01$ <b>-4%</b>	$0.558 \pm 0.05$ <b>+2%</b>
+Ours (DMA)	<b><math>0.684 \pm 0.01</math> <b>+8%</b></b>	<b><math>0.679 \pm 0.01</math> <b>+4%</b></b>	<b><math>0.601 \pm 0.05</math> <b>+10%</b></b>

Table 2. DMA recovers the components best in 11 out of 12 cases across different models and correlated components of Shapes3D. Mean  $\pm$  std. err. of DCI across all components.

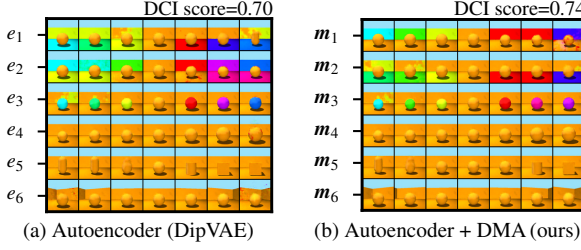


Figure 4. DMA discovers directions  $\mathbf{m}$  that control individual concepts (wall & floor color) of Shapes3D although they are confused in the original embedding space ( $e_1, e_2$ ).

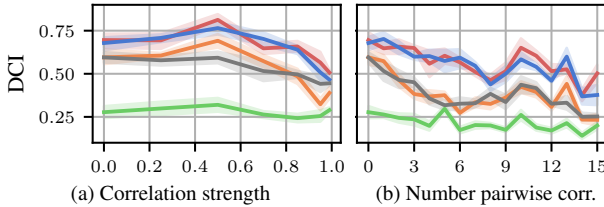


Figure 5. DMA and IMA recover the components even under strong and multiple correlations between them. ICA and PCA fail to return better components than the unit axes.

VAEs fail to recover the correlated components on their own due to their violated stochastic independence assumption (Fig. 4a). In eleven of the twelve model/correlation pairs, DMA or IMA identify better concepts than the VAE unit axes and the than PCA/ICA components with improvements of up to 29 %. This experiment shows that their concept dis-

Method	$s = 0.1$	$s = 0.15$	$s = 0.2$	$s = \infty$
unit dirs.	$0.238 \pm 0.01$	$0.244 \pm 0.01$	$0.247 \pm 0.01$	$0.286 \pm 0.02$
PCA	$0.238 \pm 0.01$	$0.376 \pm 0.03$	$0.373 \pm 0.03$	$0.343 \pm 0.03$
ICA	$0.409 \pm 0.02$	$0.309 \pm 0.02$	$0.311 \pm 0.01$	<b><math>0.652 \pm 0.00</math></b>
(Ours) IMA	$0.295 \pm 0.01$	$0.302 \pm 0.01$	$0.333 \pm 0.04$	$0.266 \pm 0.12$
(Ours) DMA	<b><math>0.435 \pm 0.01</math></b>	<b><math>0.411 \pm 0.03</math></b>	<b><math>0.392 \pm 0.02</math></b>	$0.369 \pm 0.05$

Table 3. Without correlations ( $s = \infty$ ), ICA is able to recover the components of a classification model. Under correlations, DMA works best. Mean  $\pm$  std. err. of DCI.

covery works regardless of (1) the model type and (2) the type of components correlated. On average, DMA delivers better results than IMA (+0.047), despite the generative process of Shapes3D only being roughly IMA or DMA-compliant. This indicates that the DMA criterion might be more robustly optimizable in practice. Fig. 4b visualizes the performance achieved via DMA when traversing the embedding space. It also shows that small DCI differences can mean a significant improvement. This is because (1) the metric is computed across all six components and the strong baselines already identify many concepts and (2) a perfect score of 1.0 is usually not possible due to non-linearly encoded components. We investigate other correlation strengths with similar findings in App. D.3.

### 4.3 Gaussianity and Multiple Correlations

In this section, we increase the distributional challenges to analyze whether our approaches are as distribution-agnostic as intended. We sample the components of Shapes3D from a (rotationally-symmetric) Gaussian. Additionally, we introduce correlations between multiple components to its covariance matrix. Details on how covariance matrices are constructed are given in App. C.3.

First, we study a single pair of correlated components (floor and background color) with increasing correlation strength  $\rho$ . Fig. 5a shows that the BetaVAE handles low correlations well but starts deteriorating from a strength of  $\rho > 0.5$ , along with ICA. The DCI of our methods is an average constant of +0.145 above the BetaVAE’s for  $\rho \leq 0.85$ . After this, it returns to the underlying BetaVAE’s DCI, possibly because the two components collapsed in the BetaVAE’s embedding space. For Fig. 5b, we gradually add more moderately correlated ( $\rho \approx 0.7$ ) pairs to the Gaussian’s covariance matrix until eventually all components are correlated. Again, our models show a constant benefit over the underlying BetaVAE’s DCI curve. This experiment highlights that both DMA and IMA perform well with (1) strong and (2) multiple correlations and (3) Gaussian components.

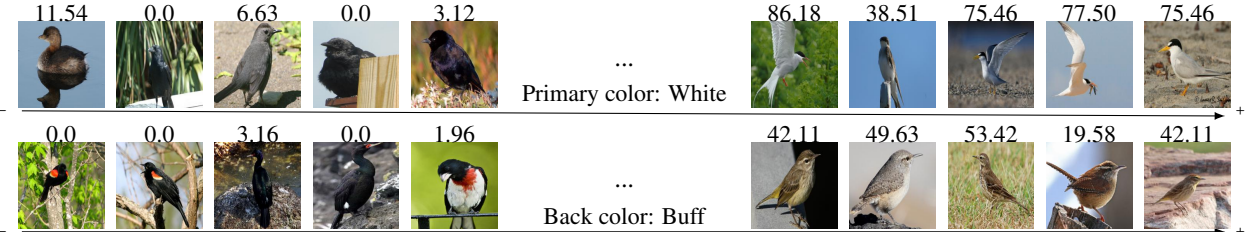


Figure 6. Each component discovered by DMA on CUB correlates with an interpretable ground truth attribute. Images are ordered by their concept scores ( $Me_i$ ), and the numbers show their ground truth annotated attribute score.

#### 4.4 Discriminative Embedding Spaces

We highlight that our approach is also applicable to classification models that were trained in a purely discriminative manner, e.g., the feature space of a CNN model. To investigate this setting, we set up an 8-class classification problem on the Shapes3D dataset, where the combination of the four binarized components object color, wall color (blue/red vs. yellow/green), shape (cylinder vs. cube) and orientation (left vs. right) determines the class as visualized in App. C.4. To make the setting even more realistic, we artificially add labeling noise close to the decision boundary, correlations as in Sec. 4.2, and a small L2-regularizer on the embeddings, keeping them in a reasonable range. We train a discriminative CNN with a  $K=6$ -dimensional embedding space.

The discriminative loss leads to a clustered distribution in the embedding space. ICA expectedly works very well in this highly non-Gaussian distribution, when no significant correlations are present which is in line with the result in Theorem 3.4. However, tables turn as we increasingly correlate the floor and background color: Starting at  $s = 0.2$ , DMA outperforms ICA and the other methods as can be seen in table Sec. 4.2. While IMA leads to better concepts over the unit directions, it does not reach the level of DMA. Overall this demonstrates that our methods are applicable to purely discriminative embedding spaces and are more robust to high levels of correlations than ICA.

#### 4.5 Real-world Concept Discovery

Last, we go beyond the traditional benchmarks and perform realistic concept discovery: We analyze the embedding space of a ResNet50 classifier [18] trained on the CUB-200-2011 [53] dataset consisting of high-resolution images of birds. This amplifies the challenges of the previous sections, i.e., a discriminative space, non-linear component dependencies of varying strengths across multiple components, and a large 512-dimensional embedding space. One restriction of this experiment is that CUB has no data-generating components to compare against, so we cannot report DCI

scores. However, we qualitatively show that DMA can deliver interpretable concepts by matching them to annotated attributes of CUB.

We apply DMA and IMA to discover  $K=30$  concepts of which the first two are shown exemplarily in Fig. 6. The images with the highest positive scores on the first component (on the right) consistently show white birds. The other end of the component comprises birds whose primary color is black. This gives a high Spearman rank correlation with the CUB attribute ‘‘primary color: white’’. The second concept is similarly interpretable. To quantify this across all  $K$  components, we provide an initial quantitative evaluation based on the Spearman rank correlation between components and attributes in App. D.6. It indicates that ICA and PCA have problems providing such components and the components identified by DMA usually correspond more closely to the attributes. While the construction of further quantitative evaluation schemes goes beyond the scope of this work, these promising results highlight that DMA also works for high-dimensional, real-world datasets.

### 5 Discussion and Conclusion

**Summary.** We proposed identifiability as a minimal requirement for concept discovery algorithms. Furthermore, we suggested the two functional paradigms of disjoint and independent mechanisms and proved that they can recover known components in visual embedding spaces. Extensive experiments confirmed that they offer substantial improvements on various generative and discriminative models and remain unaffected by distributional challenges.

**Disjoint vs. independent mechanisms.** Disjoint mechanisms are grounded in visual compositionality properties, whereas independent mechanisms are grounded in causal principles. In theory, independent mechanisms (IMA) are indisputably more general. Nevertheless, we empirically observed superior results when optimizing disjoint mechanisms (DMA) for complex datasets. We hypothesize that the disjoint loss is more robust to noisy gradient signals and does not suffer from fragile identifiability conditions (e.g.,

NEMR). Our theoretic results relying on IMA however are more broadly applicable to non-vision tasks and are a valuable starting point for further investigation.

**Outlook.** We believe our work to be a valuable step towards a rigorous formalization of concept discovery. However, the considered setup can be generalized in the future, for instance to components that are not linearly encoded. This would permit even stronger guarantees. While we have taken a technical perspective, future work is required to investigate the effect of improved concepts on upstream explanations.

## Acknowledgments

The authors thank Frederik Träuble, Luigi Gresele, and Julius von Kügelgen for insightful discussions during the early development of this project. This work was funded by the Deutsche Forschungsgemeinschaft (DFG, German Research Foundation) under Germany’s Excellence Strategy – EXC number 2064/1 – Project number 390727645. The authors thank the International Max Planck Research School for Intelligent Systems (IMPRS-IS) for supporting Michael Kirchhof.

## References

- [1] A. Akula, S. Wang, and S.-C. Zhu. Cocox: Generating conceptual and counterfactual explanations via fault-lines. In *Proceedings of the AAAI Conference on Artificial Intelligence*, volume 34, pages 2594–2601, 2020. [1](#), [2](#)
- [2] G. Alain and Y. Bengio. Understanding intermediate layers using linear classifier probes. *arXiv preprint arXiv:1610.01644*, 2016. [3](#)
- [3] D. Bau, B. Zhou, A. Khosla, A. Oliva, and A. Torralba. Network dissection: Quantifying interpretability of deep visual representations. In *Proceedings of the IEEE conference on computer vision and pattern recognition*, pages 6541–6549, 2017. [3](#)
- [4] Y. Bengio, A. Courville, and P. Vincent. Representation learning: A review and new perspectives. *IEEE transactions on pattern analysis and machine intelligence*, 35(8):1798–1828, 2013. [3](#)
- [5] A. Bisazza and C. Tump. The lazy encoder: A fine-grained analysis of the role of morphology in neural machine translation. In *Proceedings of the 2018 Conference on Empirical Methods in Natural Language Processing*, pages 2871–2876. Association for Computational Linguistics, 2018. [3](#)
- [6] C. Burgess and H. Kim. 3d shapes dataset. <https://github.com/deepmind/3dshapes-dataset/>, 2018. [6](#)
- [7] C. P. Burgess, I. Higgins, A. Pal, L. Matthey, N. Watters, G. Desjardins, and A. Lerchner. Understanding disentangling in  $\beta$ -VAE. *arXiv preprint arXiv:1804.03599*, 2018. [3](#)
- [8] R. T. Chen, X. Li, R. B. Grosse, and D. K. Duvenaud. Isolating sources of disentanglement in variational autoencoders. *Advances in neural information processing systems*, 31, 2018. [3](#), [6](#), [20](#)
- [9] T. Chen, S. Kornblith, M. Norouzi, and G. Hinton. A simple framework for contrastive learning of visual representations. In *International conference on machine learning*, pages 1597–1607. PMLR, 2020. [3](#)
- [10] Z. Chen, Y. Bei, and C. Rudin. Concept whitening for interpretable image recognition. *Nature Machine Intelligence*, 2(12):772–782, 2020. [2](#)
- [11] P. Comon. Independent component analysis, a new concept? *Signal processing*, 36(3):287–314, 1994. [2](#), [4](#), [13](#)
- [12] J. Crabbé and M. van der Schaar. Concept activation regions: A generalized framework for concept-based explanations. In *Advances in Neural Information Processing Systems*, 2022. [1](#)
- [13] C. Eastwood and C. K. Williams. A framework for the quantitative evaluation of disentangled representations. In *International Conference on Learning Representations*, 2018. [6](#), [20](#)
- [14] A. Ghorbani, J. Wexler, J. Y. Zou, and B. Kim. Towards automatic concept-based explanations. In *Advances in Neural Information Processing Systems*, volume 32, pages 9277–9286, 2019. [1](#), [2](#), [3](#)
- [15] M. W. Gondal, M. Wuthrich, D. Miladinovic, F. Locatello, M. Breidt, V. Volchkov, J. Akpo, O. Bachem, B. Schölkopf, and S. Bauer. On the transfer of inductive bias from simulation to the real world: a new disentanglement dataset. *Advances in Neural Information Processing Systems*, 32, 2019. [22](#)
- [16] I. Goodfellow, J. Pouget-Abadie, M. Mirza, B. Xu, D. Warde-Farley, S. Ozair, A. Courville, and Y. Bengio. Generative adversarial nets. *Advances in neural information processing systems*, 27, 2014. [12](#)
- [17] L. Gresele, J. von Kügelgen, V. Stimper, B. Schölkopf, and M. Besserve. Independent mechanism analysis, a new concept? In *Advances in Neural Information Processing Systems*, 2021. [3](#), [5](#), [18](#)

[18] K. He, X. Zhang, S. Ren, and J. Sun. Deep residual learning for image recognition. In *Proceedings of the IEEE conference on computer vision and pattern recognition*, pages 770–778, 2016. 8

[19] I. Higgins, L. Matthey, A. Pal, C. Burgess, X. Glorot, M. Botvinick, S. Mohamed, and A. Lerchner. beta-vae: Learning basic visual concepts with a constrained variational framework. In *International Conference on Learning Representations*, 2017. 3, 6

[20] J. Ho, A. Jain, and P. Abbeel. Denoising diffusion probabilistic models. *Advances in Neural Information Processing Systems*, 33:6840–6851, 2020. 1

[21] A. Hyvärinen and E. Oja. A fast fixed-point algorithm for independent component analysis. *Neural computation*, 9(7):1483–1492, 1997. 4

[22] A. Hyvärinen, J. Karhunen, and E. Oja. *Independent component Analysis*. John Wiley & Sons, Inc, 2001. 2

[23] A. Hyvärinen and P. Pajunen. Nonlinear independent component analysis: Existence and uniqueness results. *Neural Networks*, 12(3):429–439, 1999. ISSN 0893-6080. 2, 3

[24] A. Hyvärinen, H. Sasaki, and R. Turner. Nonlinear ica using auxiliary variables and generalized contrastive learning. In *The 22nd International Conference on Artificial Intelligence and Statistics*, pages 859–868. PMLR, 2019. 3

[25] I. T. Jolliffe. *Principal component analysis*. Springer, 2nd edition, 2002. 2, 3

[26] D. Kazhdan, B. Dimanov, M. Jamnik, P. Liò, and A. Weller. Now you see me (cme): concept-based model extraction. *AIMLAI workshop at the 29th ACM International Conference on Information and Knowledge Management (CIKM)*, 2020. 1, 2

[27] D. Kazhdan, B. Dimanov, H. A. Terre, M. Jamnik, P. Liò, and A. Weller. Is disentanglement all you need? comparing concept-based & disentanglement approaches. *RAI, WeaSul, and RobustML workshops at The Ninth International Conference on Learning Representations 2021*, 2021. 1

[28] I. Khemakhem, D. Kingma, R. Monti, and A. Hyvärinen. Variational autoencoders and nonlinear ICA: A unifying framework. In *International Conference on Artificial Intelligence and Statistics*, pages 2207–2217. PMLR, 2020. 3

[29] B. Kim, M. Wattenberg, J. Gilmer, C. Cai, J. Wexler, F. Viegas, et al. Interpretability beyond feature attribution: Quantitative testing with concept activation vectors (tcav). In *International Conference on Machine Learning*, pages 2668–2677. PMLR, 2018. 1, 2, 3

[30] H. Kim and A. Mnih. Disentangling by factorising. In *International Conference on Machine Learning*, pages 2649–2658. PMLR, 2018. 2, 3, 6, 20

[31] D. P. Kingma and M. Welling. Auto-encoding variational bayes. *arXiv preprint arXiv:1312.6114*, 2013. 1, 2, 3

[32] P. W. Koh, T. Nguyen, Y. S. Tang, S. Mussmann, E. Pierson, B. Kim, and P. Liang. Concept bottleneck models. In *International Conference on Machine Learning*, pages 5338–5348. PMLR, 2020. 1, 2

[33] A. Kumar, P. Sattigeri, and A. Balakrishnan. Variational inference of disentangled latent concepts from unlabeled observations. In *International Conference on Learning Representations*, 2018. 6, 20

[34] T. Leemann, Y. Rong, S. Kraft, E. Kasneci, and G. Kasneci. Coherence evaluation of visual concepts with objects and language. In *ICLR2022 Workshop on the Elements of Reasoning: Objects, Structure and Causality*, 2022. 1, 2, 22

[35] F. Locatello, S. Bauer, M. Lucic, G. Raetsch, S. Gelly, B. Schölkopf, and O. Bachem. Challenging common assumptions in the unsupervised learning of disentangled representations. In *International Conference on Machine Learning*, pages 4114–4124. PMLR, 2019. 3, 6, 21

[36] F. Locatello, B. Poole, G. Rätsch, B. Schölkopf, O. Bachem, and M. Tschannen. Weakly-supervised disentanglement without compromises. In *International Conference on Machine Learning*, pages 6348–6359. PMLR, 2020. 3, 6

[37] L. Muttenthaler, C. Y. Zheng, P. McClure, R. A. Vandermeulen, M. N. Hebart, and F. Pereira. VICE: Variational interpretable concept embeddings. In *Advances in Neural Information Processing Systems*, 2022. 1

[38] B. Ommer and J. M. Buhmann. Learning the compositional nature of visual objects. In *2007 IEEE Conference on Computer Vision and Pattern Recognition*, 2007. 4

[39] M. Painter, A. Prugel-Bennett, and J. Hare. Linear disentangled representations and unsupervised action estimation. In *Advances in Neural Information Processing Systems*, volume 33, pages 13297–13307. Curran Associates, Inc., 2020. 3

[40] A. Paszke, S. Gross, S. Chintala, G. Chanan, E. Yang, Z. DeVito, Z. Lin, A. Desmaison, L. Antiga, and A. Lerer. Automatic differentiation in pytorch. 2017. [1](#), [22](#)

[41] A. Ramesh, Y. Choi, and Y. LeCun. A spectral regularizer for unsupervised disentanglement. *arXiv preprint arXiv:1812.01161*, 2018. [12](#)

[42] X. Ren, T. Yang, Y. Wang, and W. Zeng. Learning disentangled representation by exploiting pretrained generative models: A contrastive learning view. In *International Conference on Learning Representations*, 2022. [2](#), [12](#)

[43] O. Russakovsky, J. Deng, H. Su, J. Krause, S. Satheesh, S. Ma, Z. Huang, A. Karpathy, A. Khosla, M. Bernstein, et al. Imagenet large scale visual recognition challenge. *International journal of computer vision*, 115:211–252, 2015. [22](#)

[44] A. Sepliarskaia, J. Kiseleva, M. de Rijke, et al. Evaluating disentangled representations. *arXiv preprint arXiv:1910.05587*, 2019. [19](#)

[45] H. Shah, P. Jain, and P. Netrapalli. Do input gradients highlight discriminative features? In M. Ranzato, A. Beygelzimer, Y. Dauphin, P. Liang, and J. W. Vaughan, editors, *Advances in Neural Information Processing Systems*, volume 34, pages 2046–2059, 2021. URL <https://proceedings.neurips.cc/paper/2021/file/0fe6a94848e5c68a54010b61b3e94b0e-Paper.pdf>. [16](#)

[46] K. Simonyan, A. Vedaldi, and A. Zisserman. Deep inside convolutional networks: Visualising image classification models and saliency maps. *arXiv preprint arXiv:1312.6034*, 2013. [16](#)

[47] D. Smilkov, N. Thorat, B. Kim, F. Viégas, and M. Wattenberg. Smoothgrad: removing noise by adding noise. In *Workshop on Visualization for Deep Learning, ICML*, 2017. [17](#)

[48] Y. Song and S. Ermon. Generative modeling by estimating gradients of the data distribution. *Advances in neural information processing systems*, 32, 2019. [1](#), [2](#)

[49] M. Sundararajan, A. Taly, and Q. Yan. Axiomatic attribution for deep networks. In *International Conference on Machine Learning*, pages 3319–3328. PMLR, 2017. [17](#)

[50] C. Szegedy, W. Zaremba, I. Sutskever, J. Bruna, D. Erhan, I. Goodfellow, and R. Fergus. Intriguing properties of neural networks. *arXiv preprint arXiv:1312.6199*, 2013. [3](#)

[51] F. Träuble, E. Creager, N. Kilbertus, F. Locatello, A. Dittadi, A. Goyal, B. Schölkopf, and S. Bauer. On disentangled representations learned from correlated data. In *International Conference on Machine Learning*, pages 10401–10412. PMLR, 2021. [2](#), [3](#), [6](#), [18](#), [19](#), [20](#), [21](#)

[52] A. Voynov and A. Babenko. Unsupervised discovery of interpretable directions in the gan latent space. In *International Conference on Machine Learning*, pages 9786–9796. PMLR, 2020. [12](#)

[53] C. Wah, S. Branson, P. Welinder, P. Perona, and S. Belongie. The Caltech-UCSD Birds-200-2011 Dataset. Technical Report CNS-TR-2011-001, 2011. [2](#), [8](#)

[54] Y. Wei, Y. Shi, X. Liu, Z. Ji, Y. Gao, Z. Wu, and W. Zuo. Orthogonal jacobian regularization for unsupervised disentanglement in image generation. In *Proceedings of the IEEE/CVF International Conference on Computer Vision*, pages 6721–6730, 2021. [12](#)

[55] T. Yang, X. Ren, Y. Wang, W. Zeng, and N. Zheng. Towards building a group-based unsupervised representation disentanglement framework. In *International Conference on Learning Representations*, 2021. [3](#)

[56] C.-K. Yeh, B. Kim, S. O. Arik, C.-L. Li, T. Pfister, and P. Ravikumar. On completeness-aware concept-based explanations in deep neural networks. In *Advances in Neural Information Processing Systems*, volume 32, 2019. [1](#), [2](#), [3](#)

[57] Y. Zheng, I. Ng, and K. Zhang. On the identifiability of nonlinear ICA with unconditional priors. In *ICLR2022 Workshop on the Elements of Reasoning: Objects, Structure and Causality*, 2022. [3](#), [5](#)

## A Additional Related Work

**Orthogonality constraints and disentanglement for generative models.** In the context of generative adversarial networks (GANs) [16], the problem of analyzing and discovering interpretable directions has been studied recently by Voynov and Babenko [52]. Ren et al. [42] propose a contrastive approach to discover interpretable directions using pretrained generative models. Wei et al. [54] have proposed an orthogonality regularization of the Jacobian, which resulted in more interpretable generative abilities. Ramesh et al. [41] constrain the right-singular vectors of a generator Jacobian to be unit directions, which corresponds to column-wise orthogonal generator Jacobians. We go beyond these works, by providing rigorous results on identifiability and by extending the scope to a much broader class of models.

## B Proofs

### B.1 Rotations Destroy Orthogonality Lemma

We start by first proving an auxiliary lemma. We show that orthogonality of Jacobians, i.e.,  $\mathbf{J}_f \mathbf{J}_f^\top = \mathbf{S}$  with a diagonal matrix  $\mathbf{S}$  will be destroyed in the general case when a rotation  $\mathbf{R}$  is applied, such that  $\mathbf{J}_{Rf} \mathbf{J}_{Rf}^\top = \mathbf{R} \mathbf{J}_f \mathbf{J}_f^\top \mathbf{R}^\top = \mathbf{R} \mathbf{S} \mathbf{R}^\top$  is not a diagonal matrix anymore.

**Lemma B.1** (Rotations destroy orthogonality patterns.). *Let  $\mathbf{S} \in \mathbb{R}^{K \times K}$  be a diagonal matrix,  $\mathbf{S} = \text{diag}(\mathbf{s})$  with diagonal entries  $s > 0$  and  $s_i \neq s_j, \forall i \neq j$ , i.e., all diagonal entries of  $\mathbf{S}$  are different and positive. Let  $\mathbf{R} \in \mathbb{R}^{K \times K}$  be any rotation matrix with  $\mathbf{R}^\top \mathbf{R} = \mathbf{I}$ . If  $\mathbf{R} \mathbf{S} \mathbf{R}^\top$  is a diagonal matrix,  $\mathbf{R}$  must be a signed permutation matrix (a permutation matrix where entries can be  $\pm 1$ ).*

**Proof.** With  $\mathbf{R} \mathbf{S} \mathbf{R}^\top = \text{diag}(\lambda_1, \dots, \lambda_K)$ , we have for each unit vector  $\mathbf{e}^{(i)}, i = 1, \dots, K$ , that

$$\mathbf{R} \mathbf{S} \mathbf{R}^\top \mathbf{e}^{(i)} = \lambda_i \mathbf{e}^{(i)}. \quad (2)$$

We can represent  $\mathbf{R}$  by its rows,  $\mathbf{R} = [\mathbf{r}_1, \dots, \mathbf{r}_K]^\top$  where each  $\mathbf{r}_i \in \mathbb{R}^K$ . In this notation,  $\mathbf{R}^\top \mathbf{e}^{(i)} = \mathbf{r}_i$ , i.e., multiplication of the transpose with a unit vector will select the row  $\mathbf{r}_i$ . This results in

$$\mathbf{R} \mathbf{S} \mathbf{r}_i = \lambda_i \mathbf{e}^{(i)} \quad (3)$$

Because  $\mathbf{R}$  is invertible and square, we can left-multiply the equation by  $\mathbf{R}^\top$ . Using  $\mathbf{R}^\top \mathbf{e}^{(i)} = \mathbf{r}_i$  again, we arrive at

$$\mathbf{S} \mathbf{r}_i = \lambda_i \mathbf{r}_i. \quad (4)$$

This implies that all  $\mathbf{r}_i$  are eigenvectors of the matrix  $\mathbf{S}$  with the eigenvalues  $\lambda_i$ . By the initial assumption,  $\mathbf{S}$  is a diagonal matrix with all-different entries  $s_i$ . The eigenvectors of such a matrix are only scaled unit vectors  $\mathbf{e}^{(j)}$ . Thus, each  $\mathbf{r}_i$  will be a scaled unit-vector. The constraint of  $\mathbf{R}$  being an orthogonal matrix enforces the  $\mathbf{r}_i$  to be mutually different unit vectors with length 1. Therefore,  $\mathbf{R}$  necessarily has the form of a signed permutation.  $\square$

Note that the converse is also true. If  $\mathbf{R}$  is a signed permutation matrix,  $\mathbf{R} \mathbf{S} \mathbf{R}^\top$  will be diagonal.

### B.2 PCA Ensures Identifiability

**Theorem B.1** (PCA identifiability). *Let  $z_k, k = 1, \dots, K$ , be uncorrelated random variables with non-zero and unequal variances. Let  $\mathbf{e} = \mathbf{D}z$ , where  $\mathbf{D} \in \mathbb{R}^{K \times K}$  is an orthonormal matrix. If an orthonormal post-hoc transformation  $\mathbf{M} \in \mathbb{R}^{K \times K}$  results in mutually uncorrelated components  $(z'_1, \dots, z'_K) = \mathbf{z}' = \mathbf{M} \mathbf{e}$ , then  $\mathbf{M} \mathbf{e} = \mathbf{P} \mathbf{S} \mathbf{z}$ , where  $\mathbf{P} \in \mathbb{R}^{K \times K}$  is a permutation and  $\mathbf{S} \in \mathbb{R}^{K \times K}$  is a matrix where  $|s_{ii}| = 1$  for  $i \in 1, \dots, K$ .*

**Proof.** Since both  $\mathbf{M}$  and  $\mathbf{D}$  are orthogonal,  $\mathbf{M} \mathbf{D} = \mathbf{Q}$  is also orthogonal. Our post-hoc transformation resulted in uncorrelated components, i.e.,  $\text{Cov}(\mathbf{Q} \mathbf{x}) = \mathbf{Q} \text{Cov}(\mathbf{x}) \mathbf{Q}^\top \Gamma$  is diagonal, where  $\Gamma$  is some diagonal matrix. Thus,  $\mathbf{Q} \text{Cov}(\mathbf{x}) \mathbf{Q}^\top$  is diagonal, too. We also know that our original components are uncorrelated with unequal variances, i.e.,  $\text{Cov}(\mathbf{x}) = \text{diag}(\mathbf{s})$  with  $s > 0$  and  $s_i \neq s_j, \forall i \neq j$ . Our helper Lemma B.1 then implies that  $\mathbf{Q}$  must be a signed permutation. Thus,  $\mathbf{z}' := \mathbf{M} \mathbf{e} = \mathbf{M} \mathbf{D} \mathbf{z} = \mathbf{Q} \mathbf{z} =: \mathbf{P} \mathbf{S} \mathbf{z}$ , where  $\mathbf{P} \in \mathbb{R}^{K \times K}$  is a permutation and  $\mathbf{S} \in \mathbb{R}^{K \times K}$  is a matrix where  $|s_{ii}| = 1$  for  $i \in 1, \dots, K$ .  $\square$

### B.3 ICA Ensures Identifiability

**Theorem B.2** (ICA identifiability). *Let  $z_k, k = 1, \dots, K$ , be independent random variables with non-zero variances where at most one component is Gaussian. Let  $\mathbf{e} = \mathbf{D}\mathbf{z}$ , where  $\mathbf{D} \in \mathbb{R}^{K \times K}$  has full rank. If a post-hoc transformation  $\mathbf{M} \in \mathbb{R}^{N \times N}$  results in mutually independent components  $(z'_1, \dots, z'_K) = \mathbf{z}' = \mathbf{M}\mathbf{e}$ , then  $\mathbf{M}\mathbf{e} = \mathbf{P}\mathbf{S}\mathbf{z}$ , where  $\mathbf{P} \in \mathbb{R}^{K \times K}$  is a permutation and  $\mathbf{S} \in \mathbb{R}^{K \times K}$  is a scaling matrix.*

**Proof.** (1) We know that  $\mathbf{z}' = \mathbf{M}\mathbf{D}\mathbf{z} =: \mathbf{C}'\mathbf{z}$ . Let us start with an additional assumption that both  $\mathbf{z}'$  and  $\mathbf{z}$  have unit variances. Then, by Comon [11, App. A.1],  $\mathbf{C}'$  must be orthonormal.

Let us recall the following result

**Theorem B.3** (Theorem 11 from Comon [11]). *Let  $\mathbf{x}$  be a vector with independent components, of which at most one is Gaussian, and whose densities are not reduced to a point-like mass. Let  $\mathbf{C}$  be an orthogonal  $K \times K$  matrix and  $\mathbf{z}$  the vector  $\mathbf{z} = \mathbf{C}\mathbf{x}$ . Then the following three properties are equivalent:*

1. *The components  $z_i$  are pairwise independent.*
2. *The components  $z_i$  are mutually independent.*
3.  *$\mathbf{C} = \mathbf{S}\mathbf{P}$  where  $\mathbf{S}$  is diagonal,  $\mathbf{P}$  is a permutation.*

Since  $\mathbf{z}$  fulfills the conditions of this theorem and  $\mathbf{z}'$  has mutually independent entries, we know that  $\mathbf{C}' = \mathbf{S}\mathbf{P}$ .

(2) We now allow arbitrary variances, i.e.,  $\text{Cov}(\mathbf{z}') = \mathbf{\Lambda}$  and  $\text{Cov}(\mathbf{z}) = \mathbf{\Gamma}$  where both covariance matrices are positive diagonal matrices.  $\mathbf{z}' = \mathbf{M}\mathbf{D}\mathbf{z} = \mathbf{C}'\mathbf{z} = \mathbf{\Lambda}^{1/2}\mathbf{\Lambda}^{-1/2}\mathbf{C}'\mathbf{\Gamma}^{1/2}\mathbf{\Gamma}^{-1/2}\mathbf{z} =: \mathbf{\Lambda}^{1/2}\mathbf{C}''\mathbf{\Gamma}^{-1/2}\mathbf{z}$ . This is equivalent to  $(\mathbf{\Lambda}^{-1/2}\mathbf{z}') = \mathbf{C}''(\mathbf{\Gamma}^{-1/2}\mathbf{z})$ . These rescaled random vectors both have unit variances, so (1) implies that  $\mathbf{C}'' = \mathbf{S}'\mathbf{P}'$ . We can plug this back into the previous equation and see that  $\mathbf{z}' = \mathbf{\Lambda}^{1/2}\mathbf{C}''\mathbf{\Gamma}^{-1/2}\mathbf{z} = \mathbf{\Lambda}^{1/2}\mathbf{S}'\mathbf{P}'\mathbf{\Gamma}^{-1/2}\mathbf{z} =: \mathbf{P}'\mathbf{S}''\mathbf{z}$ . Thus,  $\mathbf{z}' = \mathbf{M}\mathbf{e} = \mathbf{M}\mathbf{D}\mathbf{z} = \mathbf{P}'\mathbf{S}''\mathbf{z}$ , where  $\mathbf{P}' \in \mathbb{R}^{K \times K}$  is a permutation and  $\mathbf{S}'' \in \mathbb{R}^{K \times K}$  is a scaling matrix.  $\square$

### B.4 Transfer lemma

DMA and IMA are based on structures in the Jacobian of the generative process. To be able to use them in the encoder and ultimately discover concepts, we first show that if an encoder mirrors the behaviour of the generative process, up to a rotation and scale, its Jacobians must also mirror those of the generative process.

**Lemma B.2** (Transfer lemma). *Let  $\mathbf{f}$  be a faithful encoder for the generative process  $\mathbf{g}$  and further  $\mathbf{f} \circ \mathbf{g}(\mathbf{z}) = \mathbf{P}\mathbf{S}\mathbf{z} \forall \mathbf{z} \in \mathcal{Z}$  where  $\mathbf{P} \in \mathbb{R}^{K \times K}$  is a permutation and  $\mathbf{S} \in \mathbb{R}^{K \times K}$  is a diagonal matrix. Then  $\mathbf{J}_f(\mathbf{g}(\mathbf{z})) = \mathbf{P}'\mathbf{S}'\mathbf{J}_g(\mathbf{z})^\top$  where  $\mathbf{P}' \in \mathbb{R}^{K \times K}$  is a permutation and  $\mathbf{S}' \in \mathbb{R}^{K \times K}$  is a diagonal matrix.*

**Proof.** Let  $\mathbf{z} \in \mathcal{Z}$  be arbitrary.  $(\mathbf{f} \circ \mathbf{g})(\mathbf{z}) = \mathbf{P}\mathbf{S}\mathbf{z}$  implies  $\mathbf{J}_f(\mathbf{g}(\mathbf{z}))\mathbf{J}_g(\mathbf{z}) = \mathbf{P}\mathbf{S}$ . Since  $\mathbf{f}$  is faithful to  $\mathbf{g}$ ,  $\mathbf{S}$  has full rank, i.e.,  $\mathbf{S} = \text{diag}(\alpha_1, \dots, \alpha_K)$  with  $\alpha_k \in \mathbb{R}_{\neq 0}$ ,  $k = 1, \dots, K$ .

Now, let us write  $\mathbf{J}_f(\mathbf{g}(\mathbf{z})) = [\mathbf{v}_1, \dots, \mathbf{v}_K]^\top$  with  $\mathbf{v}_i \in \mathbb{R}^L$ . Similarly, we can write  $\mathbf{J}_g(\mathbf{z}) = [\mathbf{w}_1, \dots, \mathbf{w}_K]$  with  $\mathbf{w}_i \in \mathbb{R}^L$ ,  $i = 1, \dots, K$ .

Let us focus on an individual row of  $\mathbf{J}_f$ , i.e., let  $k \in \{1, \dots, K\}$  be a fixed index of a row. Since  $\mathbf{J}_f(\mathbf{g}(\mathbf{z}))\mathbf{J}_g(\mathbf{z}) = \mathbf{P}\mathbf{S}$  and  $\mathbf{P}$  is a permutation matrix with exactly one 1 per row, there is precisely one column index  $k'$  such that the  $k$ -th row and  $k'$ -th column of  $\mathbf{P}\mathbf{S}$  is non-zero. This setup allows drawing certain conclusions about the vector  $\mathbf{v}_k$ . Let  $j = 1, \dots, K$  denote an arbitrary column of  $\mathbf{P}\mathbf{S}$ . Then,

(i) if  $j = k'$ , then  $\mathbf{v}_k^\top \mathbf{w}_{k'} = \alpha_{k'} \neq 0$ . In consequence,  $\mathbf{v}_k \neq 0$ ,  $\mathbf{w}_{k'} \neq 0$  and so we can decompose  $\mathbf{v}_k = \mathbf{a}_k + \mathbf{b}_k$ , where  $\mathbf{a}_k \in \text{span}(\{\mathbf{w}_{k'}\}) \setminus \{0\}$  and  $\mathbf{b}_k \in \text{span}(\{\mathbf{w}_{k'}\})^\perp$ , where  $\perp$  denotes the orthogonal complement. Because  $\text{span}(\{\mathbf{w}_{k'}\}) = \{\mu \mathbf{w}_{k'} \mid \mu \in \mathbb{R}\}$ , we know that  $\mathbf{a}_k = \frac{\alpha_{k'}}{\|\mathbf{w}_{k'}\|^2} \mathbf{w}_{k'}$ .

(ii) if  $j \neq k'$ , then  $\mathbf{v}_k^\top \mathbf{w}_j = 0$ . With (i), it follows that  $\mathbf{b}_k \in \text{span}(\{\mathbf{w}_1, \dots, \mathbf{w}_K\})^\perp = \text{span}(\mathbf{J}_g(\mathbf{z}))^\perp$ .

Since  $f$  is faithful to  $g$ , we know that for each  $\mathbf{c} \in \text{span}(\mathbf{J}_g(z))^\perp$ ,  $\mathbf{J}_f(g(z))\mathbf{c} = \mathbf{0}$  and therefore  $\mathbf{J}_f(g(z))\mathbf{b}_k = \mathbf{0}$ . This demands that the  $k$ -th component of the product is also 0, i.e.,  $\mathbf{v}_k \mathbf{b}_k = (\mathbf{a}_k + \mathbf{b}_k)^\top \mathbf{b}_k = \mathbf{a}_k^\top \mathbf{b}_k + \mathbf{b}_k^\top \mathbf{b}_k = 0$ . By design  $\mathbf{a}_k$  and  $\mathbf{b}_k$  are orthogonal such that immediately follows  $\mathbf{b}_k = \mathbf{0}$ . Hence,  $\mathbf{v}_k = \mathbf{a}_k + \mathbf{0} = \frac{\alpha_{k'}}{\|\mathbf{w}_{k'}\|_2^2} \mathbf{w}_{k'} + \mathbf{0}$  for our selected row  $k$ . Globally, this means  $\mathbf{J}_f(g(z)) = \mathbf{P}' \mathbf{S}' \mathbf{J}_g(z)^\top$ , with some scaling matrix  $\mathbf{S}'$  and permutation matrix  $\mathbf{P}'$ .  $\square$

## B.5 Disjoint Mechanisms ensure identifiability

**Theorem B.4** (Identifiability under DMA). *Let  $g$  have disjoint mechanisms and  $f$  be a faithful encoder to  $g$ . If a full-rank post-hoc transformation  $\mathbf{M} \in \mathbb{R}^{N \times N}$  results in disjoint rows in the Jacobian  $\mathbf{M} \mathbf{J}_f(g(z))$  for some  $z \in \mathcal{Z}$ , then  $\mathbf{M} \mathbf{e} = \mathbf{P} \mathbf{S} \mathbf{z}$ , where  $\mathbf{P} \in \mathbb{R}^{K \times K}$  is a permutation and  $\mathbf{S} \in \mathbb{R}^{K \times K}$  is a scaling matrix.*

**Proof.** We know that  $f \circ g = \mathbf{D}$  and  $\mathbf{D}$  has full rank. Since  $\mathbf{M}$  also has full rank, there exists a non-singular matrix  $\mathbf{E}'$  such that  $\mathbf{M} = \mathbf{E}' \mathbf{D}^{-1}$ . We can rewrite  $\mathbf{E}' = \mathbf{S} \mathbf{E}$ , where  $\mathbf{E}$  has normalized rows and  $\mathbf{S}$  is a diagonal matrix.

Since  $\mathbf{D}^{-1} f \circ g = \mathbf{I}$  and  $g$  is DMA, we can apply the transfer lemma. It implies that  $\mathbf{D}^{-1} \mathbf{J}_f(g(z))$  has orthogonal rows.

Suppose now for contradiction that  $\mathbf{E}$  was not a permutation matrix. This means that without loss of generality the first row must contain at least two columns whose entries are not equal to zero. Since  $\mathbf{E}$  has full rank, there must be a second row with a non-zero entry in at least one of these columns. Since  $\mathbf{D}^{-1} \mathbf{J}_f(g(z_a))$  has disjoint rows,  $\mathbf{S} \mathbf{E} \mathbf{D}^{-1} \mathbf{J}_f(g(z_a)) = \mathbf{M} \mathbf{J}_f(g(z_a))$  can no longer have disjoint rows. This contradicts the assumption. Hence,  $\mathbf{E}$  must be a permutation matrix  $\mathbf{P}$ . This give  $\mathbf{z}' = \mathbf{M} \mathbf{e} = \mathbf{P} \mathbf{S} \mathbf{D}^{-1} \mathbf{D} \mathbf{z} = \mathbf{P} \mathbf{S} \mathbf{z}$ .  $\square$

## B.6 Independent Mechanisms ensure Identifiability

**Theorem B.5** (Identifiability under IMA). *Let  $g$  adhere to IMA. Let  $f$  be a faithful encoder to  $g$ . Suppose we have obtained an  $f' = \mathbf{M} f$  with a full-rank  $\mathbf{M} \in \mathbb{R}^{K \times K}$  and orthogonal rows in its Jacobian  $\mathbf{J}_{f'}(g(z))$ , i.e.,  $\mathbf{J}_{f'}(g(z)) \mathbf{J}_{f'}(g(z))^\top = \Sigma(z)$  where  $\Sigma(z)$  is diagonal. If additionally for two points  $z_a, z_b \in \mathcal{Z}$  and  $\gamma_i := \frac{\Sigma_{ii}(z_b)}{\Sigma_{ii}(z_a)}$  and  $\forall i, j = 1 \dots K, i \neq j : \gamma_i \neq \gamma_j$  (NEMR condition), then  $\mathbf{M} \mathbf{e} = \mathbf{P} \mathbf{S} \mathbf{z}$ , where  $\mathbf{P} \in \mathbb{R}^{K \times K}$  is a permutation and  $\mathbf{S} \in \mathbb{R}^{K \times K}$  is a scaling matrix.*

**Proof.** We know that  $f \circ g = \mathbf{D}$  and  $\mathbf{D}$  has full rank. Since  $\mathbf{M}$  also has full rank, there exists a non-singular matrix  $\mathbf{E}$  such that  $\mathbf{M} = \mathbf{E} \mathbf{D}^{-1}$ . We will now show that the solution set of  $\mathbf{E}$  can be constrained to be a permutation and scaling operation in three steps.

(1)  $\mathbf{J}_{f'}$  is orthogonal, i.e.,  $\Sigma(z_a) = (\mathbf{M} \mathbf{J}_f(g(z_a))) (\mathbf{M} \mathbf{J}_f(g(z_a))^\top) = (\mathbf{E} \mathbf{D}^{-1} \mathbf{J}_f(g(z_a))) (\mathbf{E} \mathbf{D}^{-1} \mathbf{J}_f(g(z_a))^\top) = \mathbf{E} (\mathbf{D}^{-1} \mathbf{J}_f(g(z_a))) (\mathbf{D}^{-1} \mathbf{J}_f(g(z_a))^\top) \mathbf{E}^\top$ . Since  $\mathbf{D}^{-1} f \circ g = \mathbf{I}$  and  $g$  is DMA, we can apply the transfer lemma and know that  $\mathbf{D}^{-1} \mathbf{J}_f(g(z_a))$  must have orthogonal rows, i.e.,  $(\mathbf{D}^{-1} \mathbf{J}_f(g(z_a))) (\mathbf{D}^{-1} \mathbf{J}_f(g(z_a))^\top) = \Gamma_a$ , where  $\Gamma_a$  is some diagonal matrix with full rank. Substituting this back into the previous term,  $\Sigma(z_a) = \mathbf{E} \Gamma_a \mathbf{E}^\top$ . The same holds for  $z_b$ , i.e.,  $\Sigma(z_b) = \mathbf{E} \Gamma_b \mathbf{E}^\top$ .

(2) We've seen in (1) that both  $\Sigma(z_a)$  and  $\Gamma_a$  are the results of quadratic forms. Hence, their entries are all positive, and strictly positive because they have full rank. Thus we can define  $\mathbf{Q} := \Sigma(z_a)^{-1/2} \mathbf{E} \Gamma_a^{1/2}$ . Due to (1),  $\mathbf{Q} \mathbf{Q}^\top = \mathbf{I}$ , i.e.,  $\mathbf{Q}$  is orthogonal. It is easy to see that  $\mathbf{E} = \Sigma(z_a)^{-1/2} \mathbf{Q} \Gamma_a^{1/2}$ . In other words,  $\mathbf{E}$  must be a (twice) scaled orthogonal matrix.

(3) From (1) we get that

$$\Sigma(z_a) \Sigma(z_b)^{-1} = \mathbf{E} \Gamma_a \mathbf{E}^\top (\mathbf{E} \Gamma_b \mathbf{E}^\top)^{-1} \quad (5)$$

$$\Sigma(z_a) \Sigma(z_b)^{-1} = \mathbf{E} \Gamma_a \Gamma_b^{-1} \mathbf{E}^{-1} \quad (6)$$

$$\mathbf{E}^{-1} \Sigma(z_a) \Sigma(z_b)^{-1} \mathbf{E} = \Gamma_a \Gamma_b^{-1} \quad (7)$$

Now we can insert the result from (2)

$$\Gamma_a^{-1/2} Q \Sigma(z_a)^{1/2} \Sigma(z_a) \Sigma(z_b)^{-1} \Sigma(z_a)^{-1/2} Q \Gamma_a^{1/2} = \Gamma_a \Gamma_b^{-1} \quad (8)$$

$$Q \Sigma(z_a)^{1/2} \Sigma(z_a) \Sigma(z_b)^{-1} \Sigma(z_a)^{-1/2} Q = \Gamma_a^{1/2} \Gamma_a \Gamma_b^{-1} \Gamma_a^{-1/2} \quad (9)$$

$$Q \Sigma(z_a) \Sigma(z_b)^{-1} Q = \Gamma_a \Gamma_b^{-1} \quad (10)$$

(11)

Due to the NEMR condition,  $\Sigma(z_a) \Sigma(z_b)^{-1}$  is a diagonal matrix with unequal positive entries. We can thus apply Lemma B.1 which implies that  $Q = PS$  where  $P$  is a permutation and  $S$  a diagonal matrix. Inserting this back into (2) gives  $E = \Sigma(z_a)^{-1/2} Q \Gamma_a^{1/2} = \Sigma(z_a)^{-1/2} P S \Gamma_a^{1/2} = P S'$ , where  $S'$  is a diagonal matrix. Hence,  $z' = M e = P S' D^{-1} D z = P S' z$ .  $\square$

In the next section, we discuss how the proofs can be turned into analytical solutions to discover the ground truth components.

## B.7 Analytical Solutions to Concept Discovery

### B.7.1 Disjoint Mechanisms

Under a perfect DMA process  $g$  and a noiseless faithful encoder  $f$  to  $g$ , we can compute an analytical solution for  $M$  that will result in an encoder  $f' = Mf$  that is compliant with the *DMA criterion*, i.e., disjoint rows in its Jacobian. Suppose we are provided with a gradient matrix of  $f$ ,  $J_f(x_a) \in \mathbb{R}^{K \times L}$ . We propose the following steps:

1. Select a submatrix  $J_{reg} \in \mathbb{R}^{K \times K}$  of  $K$  linearly independent columns in  $J_f(x_a)$ , such that  $\det(J_{reg}) \neq 0$ .
2. Compute and return  $M = J_{reg}^{-1}$
3. This will result in  $f' = Mf$  having disjoint rows in its Jacobian.

**Proof.**  $J_f(x_a)$  must be of the form  $J_f(x_a) = H^{-1} J_{f^*}(x_a)$  for such an  $M$  to exist, where  $J_{f^*}$  is the Jacobian of an encoder  $f^*$  with disjoint rows and  $H$  has full rank.  $J_{reg}$  can be written as  $J_{reg} = H^{-1} J_{f^*,reg}$ , where  $J_{f^*,reg}$  is a square submatrix of  $J_{f^*}$  with the same selected selected columns. The submatrix  $J_{f^*,reg}$  also will be of to be of full rank because it can be written as  $H J_{reg}$ , which are both full rank. Because of the DMA principle,  $J_{f^*,reg}$  again needs to be of the form  $PS$  with one component active in each column. Furthermore,  $M = J_{reg}^{-1} = (H^{-1} PS)^{-1} = S^{-1} P^{-1} H$ . As the inverses of scaling and permutation matrices have the same respective form again,  $MH^{-1} = S' P'$ . Therefore,  $f' = S' P' f^*$ , maintaining its disjoint Jacobians.

### B.7.2 Independent Mechanisms

Suppose we are given matrices  $\Sigma(z_a) = J_f(x_a) J_f(x_a)^\top = D^{-1} \Gamma_a (D^{-1})^\top$  and  $\Sigma(z_b) = J_f(x_b) J_f(x_b)^\top$ . We then apply the following steps

1.  $U = \text{inverse}((\text{cholesky}(\Sigma(z_a))))$
2.  $V = \text{eigenvectors}(U \Sigma(z_b) U^\top)$
3. return  $H = V^\top U$

The first step implies that  $U^{-1} U^{-\top} = \Sigma(z_a)$  and that  $U \Sigma(z_a) U^\top = I$ . We have thus identified the matrix  $E$  from step (2) of the identifiability proof, which has the form  $U = \Lambda^{1/2} Q \Gamma_a^{-1/2} M$ . In step two we compute  $U \Sigma(z_b) U^\top = \Lambda^{1/2} Q \Gamma_a^{-1/2} \Gamma_b \Gamma_a^{-1/2} Q^\top \Lambda^{1/2} = V R V^\top$ , where  $R$  hold the eigenvalues. Accordingly, by left and right multiplying with  $V$ , we observe that  $(V^\top U) \Sigma(z_b) (V^\top U)^\top = R$ , i.e.,  $(V^\top U)$  solves the orthogonality problem for  $\Sigma(z_b)$ . We can easily verify that  $H = V^\top U$  is also a solution for  $\Sigma(z_a)$  by computing  $V^\top U \Sigma(z_a) U^\top V = I$ . By the identifiability result,  $H = V^\top U = \Lambda P M$ , a scaled and permuted version of  $D^{-1}$ , if the additional gradient ratio condition is fulfilled with  $x_a$  and  $x_b$ .

---

**Algorithm 1:** DMA concept discovery with SGD.

---

```
Input: encoder  $f$ , images  $\{\mathbf{x}_n\}_{n=1,\dots,N}$ 
Jacobians  $\leftarrow \text{Gradient}(f, \{\mathbf{x}_n\}_{n=1,\dots,N})$ .detach()
 $M \leftarrow K$ -dim identity matrix
for  $L$  epochs,  $J_f(\mathbf{x}) \in \text{Jacobians}$  do
     $\mathbf{U} \leftarrow |\mathbf{M} \mathbf{J}_f(\mathbf{x})|$  // No absolute value operation here for IMA
     $\mathbf{U} \leftarrow \text{row-normalize } \mathbf{U}$ 
    loss  $\leftarrow \|\mathbf{U} \mathbf{U}^\top - \mathbf{I}_K\|_F$ 
    loss.backwards()
end
return  $H$ 
```

---

**Algorithm 2:** Concept discovery via Clustering of analytical solutions.

---

```
Input: encoder  $f$ , images  $\{\mathbf{x}_n\}_{n=1,\dots,N}$ , DMA/IMA flag
Jacobians  $\leftarrow \text{Gradient}(f, \{\mathbf{x}_n\}_{n=1,\dots,N})$ .detach()
for  $i \in 1 \dots N$ ,  $J_f(\mathbf{x}_i) \in \text{Jacobians}$  do
    if DMA then
         $\mathbf{M}_i \leftarrow \text{computeAnalyticalDMA}(\mathbf{J}_f(\mathbf{x}_i))$ 
    if IMA then
         $\mathbf{M}_i \leftarrow \text{computeAnalyticalIMA}(\mathbf{J}_f(\mathbf{x}_i), \mathbf{J}_f(\mathbf{x}_{i+1}))$  // IMA needs two Jacobians for  $\mathbf{M}$ 
         $\mathbf{M}_i \leftarrow \text{row-normalize } \mathbf{M}_i$ 
    end
     $\mathbf{C} \in \mathbb{R}^{2K \times K} \leftarrow \text{sphericalCluster}(\{\mathbf{M}_i[j, :] \mid i \in 1 \dots N, j \in 1, \dots, K\}, \text{n\_clusters} = 2K)$  // cluster rows in the  $\mathbf{M}_i$ , return 2K cluster centers in rows of  $\mathbf{C}$ 
     $\mathbf{M} \in \mathbb{R}^{K \times K} \leftarrow \text{mergePoles}(\mathbf{C})$  // merge rows of opposite signs
return  $\mathbf{M}$ 
```

---

## B.8 Algorithms

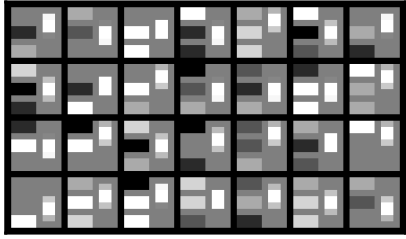
We present the SGD optimization for DMA in Algorithm 1. Note that the algorithm for IMA optimization via SGD can be obtained by just omitting the absolute value operation in the line indicated by the comment.

We further derive a clustering strategy that allows aggregating many analytical solutions, that are subject to noise. It is provided in Algorithm 2 and directly based on our identifiability theorems. They state that a scaled and permuted version of the distortion  $\mathbf{D}$  will be identified. We can compute a batch of analytical solution for data samples (one Jacobian required for DMA, two for IMA). However, when facing noise, there is a need to aggregate and average different solutions, which can only be done if the same scaling and permutations are used. The scaling can be undone easily by applying a row-wise normalization. However, we still face permutations and possibly opposite signs in the remaining rows of the matrices. Therefore, we apply an implementation of the K-Means algorithm on a unit sphere.<sup>2</sup> By this approach we identify  $2K$  cluster centers, corresponding to the directions with either positive or negative signs. We merge the directions with opposite signs by a greedy strategy: We always pick the most diametrical pair of vectors (lowest cos-distance) to be merged and only return one of them as a row in the final matrix  $\mathbf{M}$ . The two merged direction are removed from the list of cluster centers and the next directions to be merged will be selected until only  $K$  directions are in the rows of the final matrix  $\mathbf{M}$  that is returned.

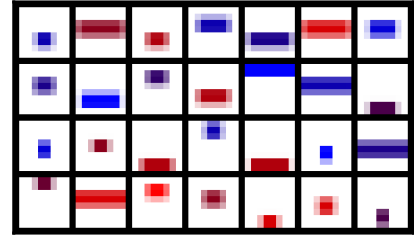
## B.9 Extending gradients to general attributions

We make an initial attempt to generalize our method, considering gradients as a simple form of attribution method. Intuitively,  $\mathbf{J}_f = \nabla_{\mathbf{x}}(f(\mathbf{x}))$  contains input gradients (termed grad in the remainder) which can be thought of as a simple form of attribution for each component [45, 46]. Thus, on a more general level, our proposed approach optimizes for the disjointness

<sup>2</sup>We use the implementation from <https://github.com/jasonlaska/spherecluster>

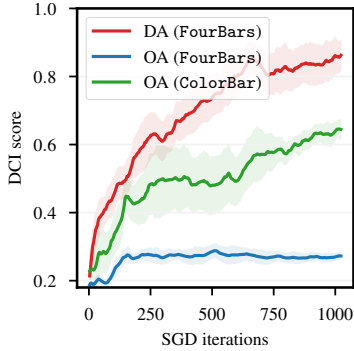


(a) Random samples in the `FourBars` dataset.

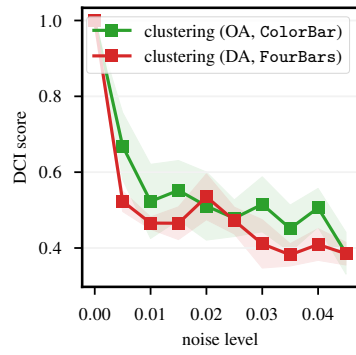


(b) Random samples in the `ColorBar` dataset.

Figure 7. Random samples drawn from the synthetic datasets.



(a) Disentangling gradients of synthetic datasets with SGD. On the `FourBars` dataset, IMA fails to iterate towards a disentangled solution, because the non-equal magnitudes condition is violated. However, IMA converges on the `ColorBar` dataset, although at a slower rate.



(b) Noise Robustness of the analytical solution. We investigate the robustness of the semi-analytical clustering approaches to noisy gradients and find that they react highly sensitive, making them unsuitable for practical applications.

Figure 8. Additional results on the synthetic datasets.

of attributions. Thus, we may use other forms of *homogeneous attributions* in place of  $\mathbf{J}_f$ . These are local attribution methods  $A_f : \mathbb{R}^L \rightarrow \mathbb{R}^{K \times L}$  for the encoder  $f$  with  $A_{Mf}(x) = M A_f(x)$  that map an instance  $x$  to a matrix of attributions for each latent dimension. Besides the above input gradients, this class contains other popular methods such as integrated gradients (IG) [49] and smoothed gradients (SG) [47] (because these methods are linear in  $f$ ). Thus, we can formulate a generalized *disjoint attributions objective*:

$$\min_{\mathbf{M}} \sum_{n=1}^N \left\| \left| \mathbf{M} A_f(x) \right| \left| \mathbf{M} A_f(x) \right|^\top - I_K \right\|_F^2. \quad (12)$$

## C Experimental Details

### C.1 Synthetic datasets

We show random samples from both datasets in Figure 7. We provide two additional graphics with the results on the synthetic datasets in Figure 8. They show that SGD exhibits a convergence behaviour as predicted by our theory and comparable to the analytical solutions. Furthermore, the results indicate that the analytical solutions is not very robust to noise.

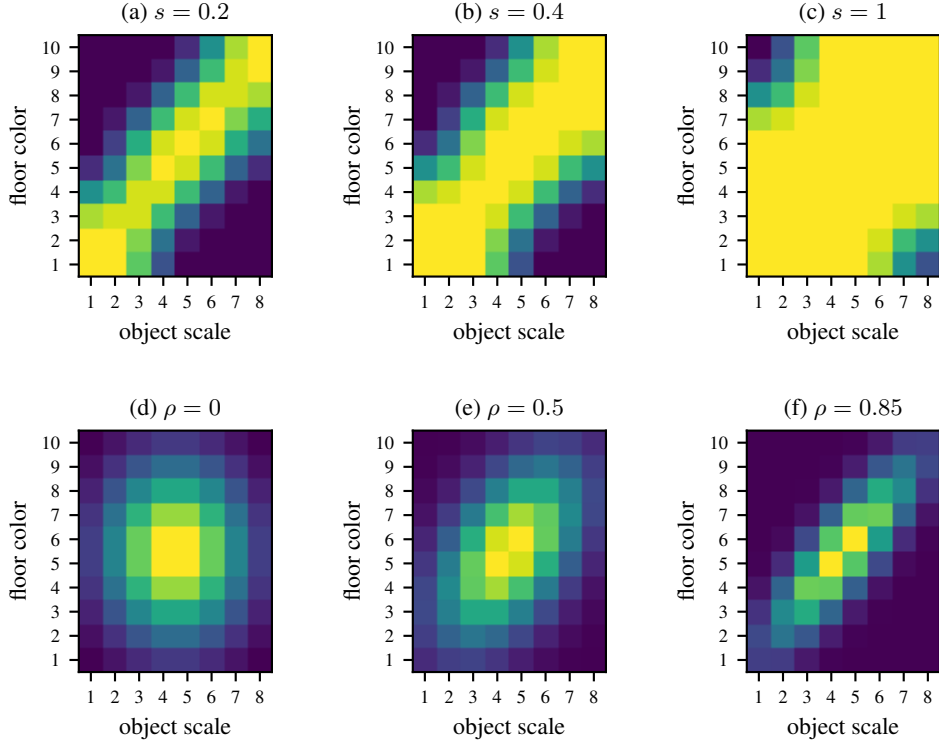


Figure 9. Exemplary correlated densities of the components floor color and object scale under the correlated sampling setup of Greselle et al. [17] (a – c) and with our Gaussian sampling (d – f). The correlation strength is indicated on top. Purple denotes a low and yellow a high density.

## C.2 Architectures

For the disentanglement models, we use the implementations provided by the open source library `disentanglement-pytorch`<sup>3</sup>. For the evaluation measures, we use the implementation of `disentanglement.lib`<sup>4</sup> with their respective default parameters. We use a simple encoder and decoder architecture, that consists of five and six feed-forward convolutional layers respectively and relies on the ReLU activation function.

## C.3 Correlated sampling

In this paper, we use two methods to introduce correlations between the ground truth components. Both methods rely on proportional resampling: We first draw a batch that has multiple times the final batch size (we use factors from 3-6 depending on the non-uniformity of the distribution), then compute the (unnormalized) probability of each sample under a given distribution over the component values, and then resample a final batch (with replacement) proportional to these probabilities.

The two methods differ in the probability distribution assigned to the component values. The first setting (used in Sec. 4.2) uses the approach of Träuble et al. [51]: As visualized in Fig. 9(a) to (c), we pick two components  $z_1$  and  $z_2$ , create the grid of possible values, and then lay a diagonal line over this grid. Along this line, we set a normal distribution with a standard deviation  $s$ . A higher  $s$  means that the distribution gives a higher probability to more component combinations of the grid,

<sup>3</sup><https://github.com/amir-abdi/disentanglement-pytorch>

<sup>4</sup>[https://github.com/google-research/disentanglement\\_lib](https://github.com/google-research/disentanglement_lib)

whereas a smaller  $s$  is more restrictive. Mathematically, it is defined by Träuble et al. [51] as:

$$p(z_1, z_2) \propto \exp\left(-\frac{(z_1 - \alpha z_2)^2}{2s^2}\right), \quad (13)$$

where  $\alpha = z_1^{\max}/z_2^{\max}$  brings the components to a same scale and  $s$  is similarly normalized to the maximum values that  $z_1$  and  $z_2$  can take. The remaining components  $z_i, i > 2$ , are marginalized out of this distribution and thus continue to be sampled uniformly at random.

This setting is limited to one pair of components and also introduces a non-Gaussian distribution over all components. To tackle these limitations and thus to make the distributional challenge harder, we use a different probability distribution in Sec. 4.3. Here, we lay a normal distribution over *all* components, i.e.,  $z \sim \mathcal{N}(\mu, \Sigma)$ , where  $\mu$  is centered in the middle of the possible values, i.e.,  $\mu = \frac{z^{\max} - z^{\min}}{2}$ .  $\Sigma$  is similarly normalized, since we decompose it into  $\Sigma = \text{diag}(\sigma^2)\Gamma$ . The vector  $\sigma \in \mathbb{R}_{>0}^K$  gives standard deviations for each component via  $\sigma^2 = \left(\frac{\mu+0.5}{2}\right)^2$  such that the distribution stretches across the grid of possible values. Note that the  $+0.5$  is because the values are assumed to be zero-indexed.  $\Gamma$  is a correlation matrix with 1 on its diagonal. In the first experiment in Sec. 4.3, we correlate only one pair of variables and set their corresponding off-diagonal entries in  $\Gamma$  to  $\rho$ . Fig. 9 (d) to (f) show the corresponding marginal distributions of these components. In the second experiment, we fill  $\Gamma$  with several correlations in the following order:

$$\begin{matrix} z_1 \\ z_2 \\ z_3 \\ z_4 \\ z_5 \\ z_6 \end{matrix} \left( \begin{array}{cccccc} 1 & 4 & 12 & 14 & 9 & \\ & 11 & 5 & 10 & 6 & \\ & & 3 & 8 & 15 & \\ & & & 13 & 7 & \\ & & & & 2 & \\ & & & & & \end{array} \right) \quad (14)$$

where the component order of the rows and columns is  $z_1 = \text{floor\_color}$ ,  $z_2 = \text{background\_color}$ ,  $z_3 = \text{object\_color}$ ,  $z_4 = \text{object\_scale}$ ,  $z_5 = \text{object\_shape}$ ,  $z_6 = \text{orientation}$ . Here, it is important to ascertain that the covariance matrix stays positive definite. Thus, we start with  $\rho = 0.7$ , check if the lowest eigenvalue of  $\Sigma$  is at least 0.2, and if not, reduce  $\rho$  by a factor of 0.9 until the eigenvalue fulfills this property. While technically it would be enough to have the smallest eigenvalue anywhere above 0, we found that 0.2 helps in numerical stability, for instance when inverting the covariance matrix to compute the multivariate normal distribution density.

#### C.4 Discriminative setup

The decision tree that is used to generate the class distribution is shown in Figure 10. It relies on 4 (binarized) components. We trained a simple CNN classifier for this problem using the cross-entropy loss. In addition to the classification loss terms, we add a regularizer  $\|z\|_2^2$ , which constrains the latent codes to not grow arbitrarily large, during training. To create a realistic setup, we subsample the dataset to follow a normal distribution as shown in Fig. 9d. We also add label noise near the decision boundary: For objects which have an orientation that is nearly centered, we follow each branch (left/right) with a probability of 50 %. With increasing left-orientedness, the probability of following the left branch increases to almost 100 % in form of a sigmoid function over the actual orientation. We follow the same procedure for the remaining features. We train the classifier for 10k iterations at a batch size of 24 and verify that it reaches an accuracy close to the best-possible one taking the mislabeled samples into account. We add correlations by increasing the chance of the the factors *obj. color* and *floor color* taking the same binary value. We use our disjoint attributions approach to find a  $H \in \mathbb{R}^{4 \times 6}$  matrix that should map the 6-dimensional latent space of the model to the four binary concepts that are used in the classification task. For the unit directions, we take the first four unit directions of the latent space, for PCA and ICA, we take the most prominent for components discovered for the evaluation with the four annotated ground truth concepts.

#### C.5 Evaluation scores

Several scores to quantify disentanglement have been proposed in the literature and often emphasize a different aspect of disentanglement [44]. Among the most common scores is the Disentanglement-Completeness-Informativeness score (DCI)

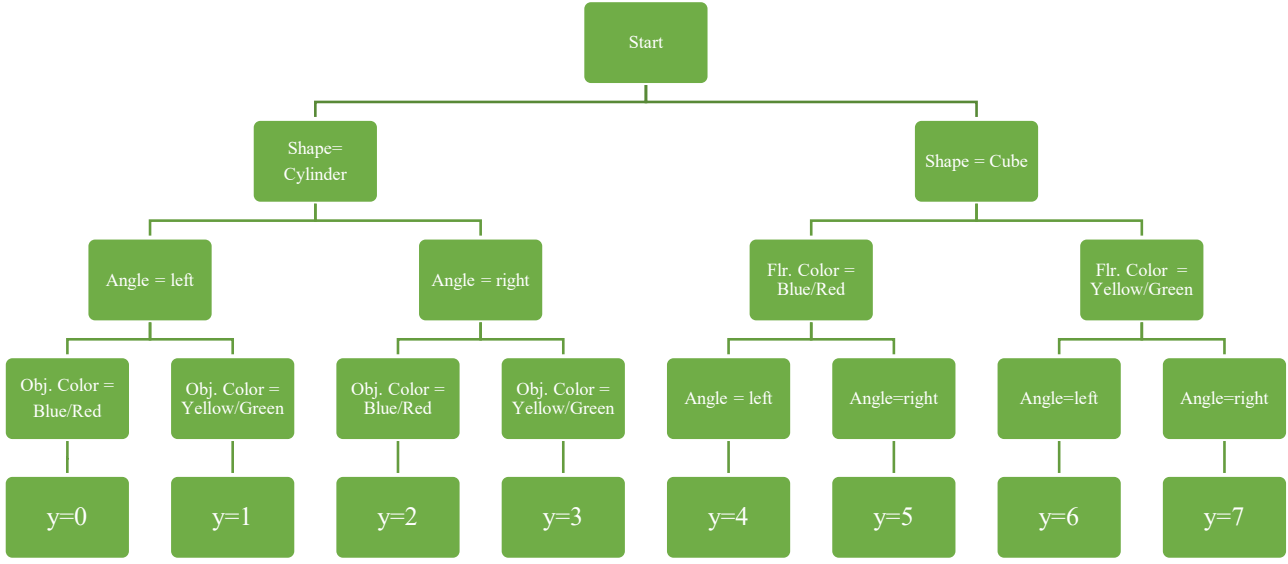


Figure 10. The decision tree setup that we use for the discriminative classification problem. Each image is assigned one out of eight class labels  $y$  according to the following decision tree.

by Eastwood and Williams [13]. In their work, they propose a metric to measure Disentanglement, that relies on training predictors  $\hat{z}_j = f_j(e)$  to predict each individual ground truth component  $z_j$  from the learned latent representation  $e$ . Furthermore, they compute normalized importance weights  $P_{ik}$  that quantify how important learned component  $e_i$  is for predicting the ground component  $z_k$ . The disentanglement metric computes a row-wise entropy over the  $P$ -matrix, which assigns a score of 1, if the learned component  $e_i$  is useful for predicting only a single factor and as score of 0, if it is equally useful for predicting all factors. Other commonly used metrics include the Mutual Information Gap (MIG) [8], Separated Attribute Predictability (SAP) [33] and the FactorVAE metric [30]. However, it is unclear which of these metrics (or if any) also provide useful results in the correlated setting Träuble et al. [51]. Therefore, to compute the reliable evaluations, we train the model (and the post-processing methods such as PCA, ICA, IMA, DMA) on the correlated dataset, but compute the metrics on samples from the full, *uncorrelated* datasets to avoid distortion in our scores. Träuble et al. noted that the DCI scores were able to discover entanglement between 2 variables [51, Figure 11, Appendix], whereas most other metrics failed even in this case. Therefore, we mainly rely on this score for our experiments but also report results for the other scores in Experiment Sec. 4.2 that show a similar picture in this appendix (Appendix D.4).

## C.6 CUB experiments

CUB-200-2011 is a fine-grained dataset containing a total of 11,788 images of 200 bird species (5994 for training and 5794 for testing). We trained a ResNet-50 with two fully-connected (fc) layers (the second fc layer served as a bottleneck layer and took 2048-dim feature vectors as input and output 512-dim ones) on CUB for 100 epochs using a SGD optimizer with an initial learning rate of 0.001. The input images were center cropped to  $224 \times 224$  pixels. Trained on a standard cross-entropy loss, the ResNet achieved a classification accuracy of on average 77.47% on five random seeds, indicating proper training. After training the classifier, we applied our proposed method to discover components in the embedding space.

CUB provides no ground-truth components since it is a real-world dataset. It does, however, contain 312 attributes semantically describing the bird classes, e.g., wing color or beak shape. These attributes have no guarantee to be complete, but they offer 312 interpretable components. This allows for an attempt to quantify whether our discovered components are interpretable and meaningful by comparing whether they match some of these interpretable ones.

Formally, we are given a set of image feature embeddings  $\{e_n\}_{n=1,\dots,N}$ ,  $e_n \in \mathbb{R}^L$  and a found matrix  $H = (h_1, \dots, h_K) \in \mathbb{R}^{L \times K}$  that contains the directions of discovered components ( $L = 512$ ,  $K = 30$ ). A score  $s_n^k$  of  $n$ -th image for the  $k$ -

Model	Ranges		
BetaVAE	$\beta \in \{1, 2, 4, 6, 8, 16\}$		
FactorVAE	$\gamma \in \{5, 8, 10, 20, 30, 40, 50, 100\}$		
BetaTCVAE	$\beta \in \{1, 2, 4, 6, 8, 10\}$		
<b>DipVAE</b>	$\lambda_{od} \in \{\text{MP23D, r10, 20, 50}\}$		
Correlated	background & object color	background & robot arm dof-1 & robot arm dof-2	
<b>BetaVAE</b>	$0.340 \pm 0.027$	$0.277 \pm 0.026$	$0.300 \pm 0.046$
+PCA	$0.116 \pm 0.008$	$0.174 \pm 0.021$	$0.154 \pm 0.015$
+ICA	$0.237 \pm 0.042$	$0.205 \pm 0.023$	$0.180 \pm 0.021$
+Ours (IMA)	<b><math>0.355 \pm 0.033</math></b>	<b><math>0.349 \pm 0.015</math></b>	<b><math>0.337 \pm 0.038</math></b>
+Ours (DMA)	$0.334 \pm 0.025$	$0.317 \pm 0.028$	$0.278 \pm 0.030$
<b>FactorVAE</b>	<b><math>0.205 \pm 0.022</math></b>	<b><math>0.239 \pm 0.017</math></b>	$0.171 \pm 0.005$
+PCA	$0.179 \pm 0.010$	$0.234 \pm 0.012$	$0.171 \pm 0.006$
+ICA	$0.066 \pm 0.009$	$0.090 \pm 0.006$	$0.073 \pm 0.011$
+Ours (IMA)	$0.201 \pm 0.019$	$0.226 \pm 0.010$	<b><math>0.191 \pm 0.011</math></b>
+Ours (DMA)	$0.184 \pm 0.013$	$0.218 \pm 0.016$	$0.180 \pm 0.013$
<b>BetaTCVAE</b>	<b><math>0.383 \pm 0.022</math></b>	<b><math>0.359 \pm 0.026</math></b>	<b><math>0.309 \pm 0.036</math></b>
+PCA	$0.356 \pm 0.022$	$0.328 \pm 0.017$	$0.295 \pm 0.038$
+ICA	$0.245 \pm 0.041$	$0.260 \pm 0.024$	$0.170 \pm 0.045$
+Ours (IMA)	$0.323 \pm 0.025$	$0.316 \pm 0.029$	$0.271 \pm 0.033$
+Ours (DMA)	$0.327 \pm 0.027$	$0.325 \pm 0.025$	$0.272 \pm 0.033$
<b>DipVAE</b>	$0.235 \pm 0.019$	$0.181 \pm 0.049$	$0.232 \pm 0.040$
+PCA	$0.090 \pm 0.005$	$0.088 \pm 0.028$	$0.091 \pm 0.011$
+ICA	$0.234 \pm 0.019$	$0.180 \pm 0.048$	$0.232 \pm 0.041$
+Ours (IMA)	$0.230 \pm 0.022$	$0.182 \pm 0.048$	$0.230 \pm 0.042$
Ours (DMA)	<b><math>0.249 \pm 0.026</math></b>	<b><math>0.188 \pm 0.049</math></b>	<b><math>0.253 \pm 0.051</math></b>

Table 5. Mean  $\pm$  std. err. of the DCI scores (across all components of the dataset) of several models and post-hoc methods applied to their embeddings. Columns show which pair of components was correlated during training.

th discovered component can be calculated by projecting the feature embeddings on that component direction, i.e.,  $s_n^k = \langle e_n, h_k \rangle$ . One pitfall is that  $s_n^k$  can be negative, indicating, e.g., a non-black bird for the component "primary color: black", but this opposite attribute is usually encoded in a separate attribute in CUB, e.g., "primary color: white". Thus, we separate the negative and positive values into two components (where we set values of the opposite sign to 0), resulting in  $2 \cdot K$  positive scores for each image.

To compare these component scores with the attributes, we make use of the numerical attribute values provided in CUB. First, we average the  $2 \cdot K$  component values of all images of a class, to be comparable with the class-wise attributes provided by CUB. This gives us a numerical  $2 \cdot K$  dimensional component description and a 312 dimensional attribute description per class. Now, we match the discovered components to the attributes. We compare each discovered component to each attributes via the Spearman's rank correlation coefficient and consider the attribute with the highest score to match the component. These are the matches used in Sec. 4.5. We further use the (average) Spearman's rank correlation across all components to their best-matching attributes to quantify how well the components match to interpretable attributes in Appendix D.6.

## C.7 Hyperparameters for the disentanglement models

We orient our hyperparameter ranges by the works of Locatello et al. [35], Träuble et al. [51]. The exact ranges are provided in Tab. 4. We find the best hyperparameters in the ranges for each correlation strength/dataset/model triple separately. Then we train five models from independent seeds to run our experiments. We use the Adam optimizer for all model with a learning rate of  $10^{-4}$ , batch size of 64 and train for 300k iterations (equiv. to 40 epochs on Shapes3D).

For the optimization of the post-hoc disentanglement problem, we use slightly different hyperparameters. We use the RMSProp optimizer with learning rate of  $10^{-3}$  and a batch size of 48.



No.	Top Concepts ( <b>jack-o-lantern</b> )	Weight	Act.
2	candles, burning, flame, fire, fires (rating: 2.28)	0.24	1.92
4	batting helmet, patella, spinal column, hindquarter, passenger car (rating: 2.09)	0.14	1.68
8	birds, flamingo, new world blackbird, duck, october (rating: 2.04)	0.22	0.74

No.	Top Concepts ( <b>traffic light</b> )	Weight	Act.
1	stoplight, traffic light, traffic, boulevard, transportation system (rating: 2.04)	0.28	1.04
2	candles, burning, flame, fire, fires (rating: 2.28)	0.15	1.92
4	towers, buildings, condos, lamppost, building (rating: 1.93)	0.19	1.18

**candles, burning, flame, fire, fires (rating: 2.28)**

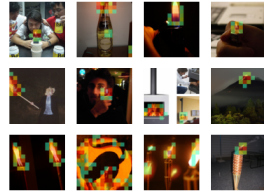


Figure 11. Original local conceptual explanation of the missclassification. We find that the most activating concept “candles, burning, flame...” activates for very dark images. This concept is also highly activated for the traffic light example. We cleared up the description of the concepts for the motivational figure.

## C.8 Details on the introductory example

The introductory example is inspired by a real explanation generated for a missclassification of the ResNet50 model pre-trained on the Imagenet [43] dataset delivered with the popular `pytorch` [40] package. Using the approach devised by [34], we use the individual neurons of the classifier’s last-layer as concepts and describe them by words. We obtain the conceptual explanation shown in Figure 11. We simplify the explanation for the motivational figure and give the concepts relatable names. However, the gist of the example stays the same.

## D Additional results

### D.1 Reconstruction quality

As a check, we investigate the reconstruction quality of the disentanglement models. For the 3D shapes, the reconstruction is very high, but we observe some more serious reconstruction errors on the MPI-3d dataset: (Appendix D.2). Figures 12 and 13 show the original images on the left and the reconstructions of a randomly chosen BetaVAE on the right. On Shapes3D, the BetaVAE is able to reconstruct the image from its embedding representation. On MPI3D-real, it is able to reconstruct the big image parts shared across many pictures (ground, background stripe and background), but becomes blurry in the smaller and more nuanced robot arm and object shapes. This indicates that the information on these components might not be stored in the embedding space and is thus hardly disentangable. A longer training (800k instead of 300k iterations) did not resolve the issue. The issue might arise, following Gondal et al. [15], because the input images were scaled down to 64x64 pixels making the detailed objects hard to perceive, and because the same architecture as in the Shapes3D experiments was used, which might not be expressive enough.

### D.2 Results for the MPI-3D dataset

In addition to 3Dshapes, with use the challenging MPI3D-real dataset [15], which consists of realistic images of a moving robot arm. It is by far more challenging, as the component is only present in a small portion of the images, and the data consists of real photographs. We report the results on this dataset in Table 5. We saw low disentanglement scores of both the base and post-hoc models on MPI3D-real compared to the performance on Shapes3D. This implies that the embedding spaces of the VAEs was not trained well. In fact, this is supported by the reconstruction quality considerations on both Shapes3D and MPI3D-real. Because our approaches are based on the given embeddings, they also struggle when they incorrectly reflect the sample.

### D.3 Correlation strengths and attribution methods in first experiment

In this section we provide additional ablations for the rectification experiment in Sec. 4.2. We investigate the impact of the choice of attribution method and the correlation strength  $s$ . The values (DCI scores) are shown in Tab. 8. As expected, our approach offers the highest gains over the baseline when the correlation is higher. Starting at  $s = 0.4$ , our runs start to reliably

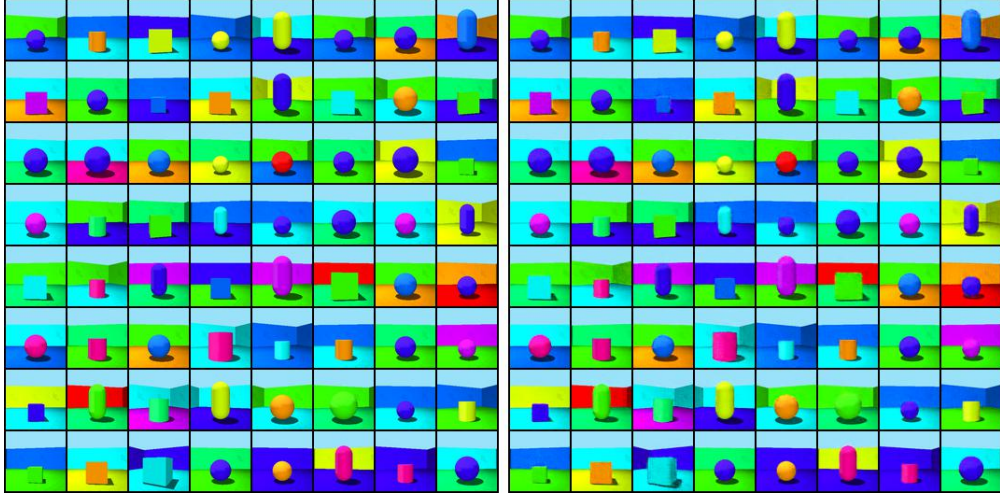


Figure 12. Random example images (left) and their reconstructions (right) of a BetaVAE on Shapes3D.

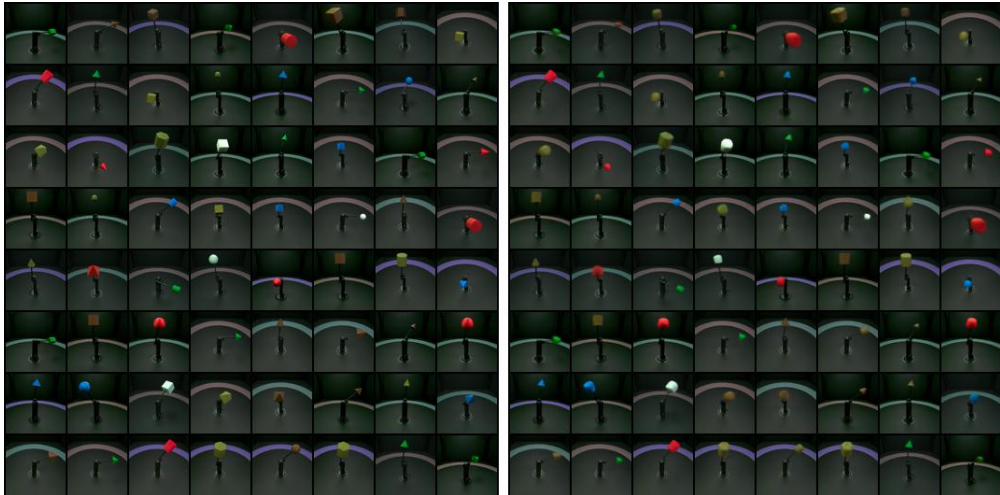


Figure 13. Random example images (left) and their reconstructions (right) of a BetaVAE on MPI3D-real.

outperform the baselines. Regarding the attributions, there is no clear picture, but Grad and SG seem to yield good results more stably across runs. DMA usually outperforms IMA, which supports our theoretical results on identifiability.

#### D.4 Further disentanglement metrics and algorithm

Tables 9 – 11 show the results of the experiment in Sec. 4.2 measured in the alternative metrics MIG, FactorVAE and SAP score. For MIG, we see similar results as for DCI in Section 4.2 and in Table 5. The results in FactorVAE and SAP score are slightly inferior but our approach still improves over the baseline in many setups.

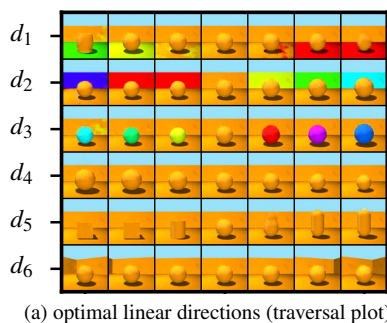
We add the clustering approach given in Algorithm 2 to the set of competitors. The results are given in Table 6. While it is able to beat the baselines for 8/12 setups, it does not reach the level of the DMA method with SGD optimization. We also compute the disentanglement only on the two correlated components for the first pair of factors in Table 7. This emphasized the improvement introduced by our IMA and DMA approaches.

Dataset	Shapes3D		
	floor vs. background	orientation vs. background	orientation vs. size
<b>BetaVAE</b>	$0.497 \pm 0.028$	$0.581 \pm 0.044$	$0.491 \pm 0.049$
+PCA	$0.263 \pm 0.028$	$0.310 \pm 0.025$	$0.324 \pm 0.041$
+ICA	$0.574 \pm 0.040$	$0.540 \pm 0.080$	$0.577 \pm 0.038$
+IMA-SGD	<u><math>0.617 \pm 0.018</math></u>	<u><math>0.602 \pm 0.050</math></u>	<u><math>0.579 \pm 0.032</math></u>
+IMA-Clust	<u><math>0.510 \pm 0.255</math></u>	<u><math>0.473 \pm 0.236</math></u>	<u><math>0.545 \pm 0.273</math></u>
+DMA-SGD	<b><math>0.641 \pm 0.031</math></b>	<b><math>0.624 \pm 0.055</math></b>	<b><math>0.627 \pm 0.031</math></b>
<b>FactorVAE</b>	$0.507 \pm 0.105$	$0.502 \pm 0.076$	$0.712 \pm 0.010$
+PCA	$0.358 \pm 0.075$	$0.474 \pm 0.051$	$0.556 \pm 0.029$
+ICA	$0.294 \pm 0.070$	$0.263 \pm 0.053$	$0.340 \pm 0.034$
+IMA-SGD	<u><math>0.551 \pm 0.040</math></u>	<u><math>0.498 \pm 0.034</math></u>	<u><math>0.595 \pm 0.051</math></u>
+IMA-Clust	$0.248 \pm 0.124$	$0.352 \pm 0.176$	$0.235 \pm 0.117$
+DMA-SGD	<b><math>0.584 \pm 0.047</math></b>	<b><math>0.510 \pm 0.055</math></b>	$0.556 \pm 0.038$
<b>BetaTCVAE</b>	$0.619 \pm 0.008$	$0.613 \pm 0.041$	$0.659 \pm 0.005$
+PCA	$0.400 \pm 0.030$	$0.421 \pm 0.068$	$0.450 \pm 0.065$
+ICA	$0.540 \pm 0.023$	$0.497 \pm 0.036$	$0.627 \pm 0.023$
+IMA-SGD	<u><math>0.623 \pm 0.021</math></u>	<u><math>0.652 \pm 0.028</math></u>	$0.638 \pm 0.037$
+IMA-Clust	<u><math>0.647 \pm 0.323</math></u>	<u><math>0.633 \pm 0.316</math></u>	<u><math>0.659 \pm 0.330</math></u>
+DMA-SGD	<b><math>0.666 \pm 0.010</math></b>	<b><math>0.664 \pm 0.023</math></b>	<b><math>0.748 \pm 0.026</math></b>
<b>DipVAE</b>	$0.631 \pm 0.018$	$0.652 \pm 0.017$	$0.548 \pm 0.036$
+PCA	$0.158 \pm 0.013$	$0.160 \pm 0.020$	$0.170 \pm 0.022$
+ICA	$0.630 \pm 0.018$	$0.651 \pm 0.017$	$0.542 \pm 0.033$
+IMA-SGD	<u><math>0.644 \pm 0.019</math></u>	$0.624 \pm 0.014$	<u><math>0.558 \pm 0.051</math></u>
+IMA-Clust	<u><math>0.639 \pm 0.319</math></u>	$0.613 \pm 0.306$	$0.521 \pm 0.260$
+DMA-SGD	<b><math>0.684 \pm 0.009</math></b>	<b><math>0.679 \pm 0.013</math></b>	<b><math>0.601 \pm 0.055</math></b>

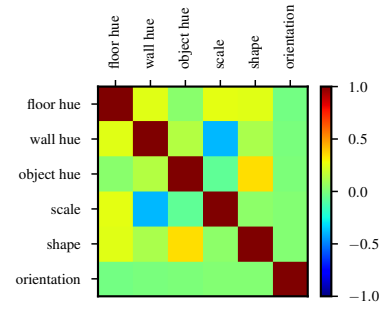
Table 6. Mean  $\pm$  std. err. of the DCI scores of four post-hoc methods applied to the embedding spaces of four disentanglement models on two datasets with different pairs of correlated variables. We compare our IMA and DMA methods to the clustering strategy that relies on analytical solutions.

Dataset	Shapes3D
Correlated factors	floor vs. background
<b>BetaVAE</b>	$0.579 \pm 0.089$
+PCA	$0.291 \pm 0.033$
+ICA	$0.435 \pm 0.076$
+IMA-SGD	<u><math>0.738 \pm 0.072</math></u>
+DMA-SGD	<b><math>0.868 \pm 0.025</math></b>
<b>FactorVAE</b>	$0.684 \pm 0.163$
+PCA	$0.526 \pm 0.136$
+ICA	$0.363 \pm 0.097$
+IMA-SGD	<u><math>0.779 \pm 0.063</math></u>
+DMA-SGD	<b><math>0.847 \pm 0.072</math></b>
<b>BetaTCVAE</b>	$0.589 \pm 0.005$
+PCA	$0.388 \pm 0.046$
+ICA	$0.609 \pm 0.065$
+IMA-SGD	<b><math>0.876 \pm 0.027</math></b>
+DMA-SGD	<u><math>0.754 \pm 0.127</math></u>
<b>DipVAE</b>	$0.615 \pm 0.114$
+PCA	$0.429 \pm 0.169$
+ICA	$0.585 \pm 0.024$
+IMA-SGD	<b><math>0.798 \pm 0.099</math></b>
+DMA-SGD	<u><math>0.782 \pm 0.009</math></u>

Table 7. Mean  $\pm$  std. err. of the DCI scores of four post-hoc methods applied to the embedding spaces of four disentanglement models on two datasets with different pairs of correlated variables. The DCI is computed across **the two correlated components** of the dataset.



(a) optimal linear directions (traversal plot)



(b) Cosines of the linear directions

Figure 14. Empirical results for linear entanglement. For the model shown in Fig. 4 (trained on correlated data), we observe almost perfect linear entanglement, i.e., that  $f \circ g = D$ : (a) There exist linear directions  $d_1$  to  $d_6$  in  $f$ 's embedding space that encode the individual components. (b) However, these directions are not necessarily orthogonal; they can be entangled as testified by non-zero cosine distances between them. See Fig. 15 for additional results.

## D.5 Qualitative results on Shapes3D

In this section, we want to show another traversal plot like the one in Fig. 4 and more thoroughly analyze its latent space. We chose another architecture (BetaTCVAE) and  $s = 0.2$  with the usual correlated factors *floor color* and *background color*. Out of the 5 independent runs, we selected the one with the highest DCI score (of the base model) for the analysis.

Model Correlation	BetaVAE			FactorVAE			BetaTCVAE			DIPVAEI		
	$s = 0.2$	$s = 0.4$	$s = \infty$	$s = 0.2$	$s = 0.4$	$s = \infty$	$s = 0.2$	$s = 0.4$	$s = \infty$	$s = 0.2$	$s = 0.4$	$s = \infty$
unit dirs.	0.666 ±0.030	0.497 ±0.028	0.650 ±0.049	0.441 ±0.065	0.507 ±0.105	0.651 ±0.087	0.580 ±0.022	0.619 ±0.008	0.504 ±0.056	0.686 ±0.072	0.631 ±0.018	0.868 ±0.052
PCA	0.287 ±0.010	0.263 ±0.028	0.357 ±0.024	0.312 ±0.048	0.358 ±0.075	0.484 ±0.064	0.341 ±0.018	0.400 ±0.030	0.396 ±0.061	0.266 ±0.029	0.158 ±0.013	0.215 ±0.037
ICA	0.394 ±0.099	0.574 ±0.040	0.674 ±0.012	0.193 ±0.052	0.294 ±0.070	0.390 ±0.109	0.516 ±0.019	0.540 ±0.023	<b>0.642</b> ±0.007	0.672 ±0.073	0.630 ±0.018	<b>0.870</b> ±0.049
Grad (IMA)	0.638 ±0.067	0.617 ±0.018	0.556 ±0.109	0.478 ±0.046	0.551 ±0.040	<b>0.666</b> ±0.041	0.548 ±0.035	0.623 ±0.021	0.551 ±0.038	0.705 ±0.062	0.644 ±0.019	0.794 ±0.043
IG (IMA)	0.702 ±0.035	0.460 ±0.128	0.578 ±0.117	0.470 ±0.035	0.511 ±0.042	0.581 ±0.066	0.619 ±0.024	0.533 ±0.006	0.612 ±0.024	0.650 ±0.072	0.605 ±0.006	0.701 ±0.045
SG (IMA)	0.677 ±0.037	0.438 ±0.127	0.609 ±0.131	0.475 ±0.042	0.561 ±0.040	0.644 ±0.055	0.533 ±0.028	0.620 ±0.021	0.559 ±0.040	0.698 ±0.060	0.642 ±0.017	0.785 ±0.046
Grad (DMA)	0.645 ±0.067	<b>0.641</b> ±0.031	<b>0.690</b> ±0.062	0.547 ±0.056	0.584 ±0.047	0.385 ±0.169	<b>0.629</b> ±0.033	0.666 ±0.010	0.598 ±0.057	<b>0.717</b> ±0.059	<b>0.684</b> ±0.009	0.857 ±0.037
IG (DMA)	0.645 ±0.076	0.530 ±0.106	0.548 ±0.114	<b>0.573</b> ±0.046	<b>0.615</b> ±0.045	0.631 ±0.128	0.607 ±0.028	0.624 ±0.021	0.584 ±0.039	0.703 ±0.073	0.659 ±0.008	0.771 ±0.029
SG (DMA)	<b>0.711</b> ±0.040	0.593 ±0.094	0.633 ±0.062	0.506 ±0.057	0.600 ±0.027	0.644 ±0.066	0.628 ±0.033	<b>0.670</b> ±0.014	0.595 ±0.059	0.716 ±0.059	0.682 ±0.010	0.851 ±0.036

Table 8. Mean ± std. err. of the DCI score of the experiments in Sec. 4.2 for the first correlated component pair (*floor* vs *background* color) in Shapes3D, as an ablation study with further correlations strengths and attribution methods (see Appendix B.9). We observe only small differences between attribution methods, with plain Grad and SG performing best in the DMA setting.

**Linear entanglement matrix.** To study which factors are encoded in which latent dimension, we compute a matrix of linear entanglement. By our linear entanglement hypothesis,  $\mathbf{z}' = \mathbf{D}\mathbf{z}$ , where the matrix  $\mathbf{D} = [\mathbf{d}_1, \dots, \mathbf{d}_K] \in \mathbb{R}^{K \times K}$  contains the directions  $\mathbf{d}_i \in \mathbb{R}^K$ , in which the ground truth concepts are encoded. Changing the component  $i$  (entry  $\mathbf{z}_i$ ) by one unit will change the resulting embedding by  $\mathbf{d}_i$ . To find these  $\mathbf{d}_i$ , we take the factors at the origin of the traversal plot and alter only a single component  $i$ . We then encode the image corresponding to that change, and measure the change in embeddings to find the linear direction  $\mathbf{d}_i$  that the corresponding component is encoded in (to be precise, we sample several changes and take the largest eigenvector of the embedding changes covariance). Thus, we can estimate the matrix  $\mathbf{D}$ . An example is shown in Fig. 14a and provides evidence that linear entanglement is possible when training autoencoder models from correlated data.

To estimate which factors are changing when a unit direction of the (plain or postprocessed) embedding space is followed (a change in  $\mathbf{z}'_i$ ), we can invert the equation to  $\mathbf{z} = \mathbf{D}^{-1}\mathbf{z}'$ . The columns in  $\mathbf{D}^{-1}$  correspond to the change in ground truth components that going one unit in the latent space coordinate  $i$  will entail. We refer to this matrix  $\mathbf{D}^{-1}$ , that shows which ground truth components will be altered by moving along one latent dimension as *linear entanglement matrix*.

Figure 15 shows the traversals along with the corresponding linear entanglement matrices that correspond well to the changes observed. For the plain method, the components that were correlated are deeply entangled (upper line). However, our method (DMA, SG, lower line) is able to separate them well, which is testified both by the traversal and the linear disentanglement matrix.

## D.6 Further results on CUB

In Tab. 12, we report the quantitative comparison on CUB introduced in Appendix C.6 of our methods with PCA, ICA, and a baseline of randomly sampled directions. ICA failed to discover meaningful components, while PCA was only capable of discovering very few high-variance ones in the beginning, but begins to fail for  $K > 10$ . This is possibly because in PCA, the directions are required to be orthogonal. Surprisingly, both PCA and ICA were not much better than the random baseline. Our method constantly discovered components and surpassed all three baselines. In particular, our method (DMA) with Integrated Gradient attributions instead of plain gradients (see Appendix B.9) leads to good performance. This leads us to the hypotheses that for high-dimensional data, (1) the disjointness principle is required to identify solutions and (2) that the gradients need

Dataset		Shapes3D			MPI3D-real		
Correlated factors	floor vs. background	orientation vs. background	orientation vs. size	background vs. object color	background vs. robot arm dof-1	robot arm dof-1 vs. robot arm dof-2	
<b>BetaVAE</b>	0.309 $\pm$ 0.031	0.426 $\pm$ 0.043	0.335 $\pm$ 0.059	0.232 $\pm$ 0.022	0.185 $\pm$ 0.031	<b>0.196 <math>\pm</math> 0.034</b>	
+PCA	0.111 $\pm$ 0.031	0.101 $\pm$ 0.009	0.092 $\pm$ 0.031	0.095 $\pm$ 0.010	0.105 $\pm$ 0.023	0.123 $\pm$ 0.033	
+ICA	0.360 $\pm$ 0.040	0.324 $\pm$ 0.054	0.277 $\pm$ 0.036	0.155 $\pm$ 0.025	0.163 $\pm$ 0.014	0.071 $\pm$ 0.014	
+Ours (IMA)	0.511 $\pm$ 0.029	0.437 $\pm$ 0.044	0.502 $\pm$ 0.030	<b>0.239 <math>\pm</math> 0.021</b>	<b>0.229 <math>\pm</math> 0.022</b>	0.187 $\pm$ 0.039	
+Ours (DMA)	<b>0.594 <math>\pm</math> 0.023</b>	<b>0.485 <math>\pm</math> 0.057</b>	<b>0.545 <math>\pm</math> 0.034</b>	0.193 $\pm$ 0.036	0.092 $\pm$ 0.038	0.080 $\pm$ 0.015	
<b>FactorVAE</b>	0.297 $\pm$ 0.084	0.319 $\pm$ 0.076	<b>0.423 <math>\pm</math> 0.018</b>	0.079 $\pm$ 0.001	0.103 $\pm$ 0.020	0.080 $\pm$ 0.010	
+PCA	0.202 $\pm$ 0.057	0.135 $\pm$ 0.028	0.235 $\pm$ 0.036	<b>0.111 <math>\pm</math> 0.006</b>	<b>0.122 <math>\pm</math> 0.011</b>	<b>0.107 <math>\pm</math> 0.009</b>	
+ICA	0.199 $\pm$ 0.061	0.106 $\pm$ 0.025	0.078 $\pm$ 0.021	0.018 $\pm$ 0.008	0.061 $\pm$ 0.015	0.069 $\pm$ 0.015	
+Ours (IMA)	<b>0.337 <math>\pm</math> 0.033</b>	<b>0.322 <math>\pm</math> 0.056</b>	0.288 $\pm$ 0.092	0.070 $\pm$ 0.014	0.086 $\pm$ 0.018	0.039 $\pm$ 0.014	
+Ours (DMA)	0.276 $\pm$ 0.036	0.217 $\pm$ 0.064	0.213 $\pm$ 0.036	0.046 $\pm$ 0.021	0.045 $\pm$ 0.016	0.048 $\pm$ 0.015	
<b>BetaTCVAE</b>	0.333 $\pm$ 0.008	0.400 $\pm$ 0.046	0.402 $\pm$ 0.017	<b>0.279 <math>\pm</math> 0.025</b>	<b>0.223 <math>\pm</math> 0.030</b>	0.201 $\pm$ 0.039	
+PCA	0.249 $\pm$ 0.033	0.145 $\pm$ 0.039	0.184 $\pm$ 0.062	0.265 $\pm$ 0.019	0.203 $\pm$ 0.028	<b>0.213 <math>\pm</math> 0.035</b>	
+ICA	0.390 $\pm$ 0.031	0.276 $\pm$ 0.043	0.346 $\pm$ 0.072	0.199 $\pm$ 0.040	0.158 $\pm$ 0.038	0.170 $\pm$ 0.033	
+Ours (IMA)	0.484 $\pm$ 0.025	0.490 $\pm$ 0.033	0.526 $\pm$ 0.036	0.092 $\pm$ 0.029	0.071 $\pm$ 0.029	0.041 $\pm$ 0.014	
+Ours (DMA)	<b>0.525 <math>\pm</math> 0.014</b>	<b>0.540 <math>\pm</math> 0.021</b>	<b>0.620 <math>\pm</math> 0.024</b>	0.120 $\pm$ 0.037	0.122 $\pm$ 0.044	0.075 $\pm$ 0.028	
<b>DipVAE</b>	0.493 $\pm$ 0.032	0.481 $\pm$ 0.020	0.433 $\pm$ 0.044	0.138 $\pm$ 0.020	0.099 $\pm$ 0.040	<b>0.143 <math>\pm</math> 0.045</b>	
+PCA	0.063 $\pm$ 0.006	0.086 $\pm$ 0.027	0.108 $\pm$ 0.014	0.054 $\pm$ 0.016	0.042 $\pm$ 0.011	0.064 $\pm$ 0.010	
+ICA	0.495 $\pm$ 0.032	0.438 $\pm$ 0.053	0.224 $\pm$ 0.026	0.138 $\pm$ 0.023	0.096 $\pm$ 0.040	0.139 $\pm$ 0.047	
+Ours (IMA)	0.512 $\pm$ 0.042	0.425 $\pm$ 0.036	0.465 $\pm$ 0.049	<b>0.146 <math>\pm</math> 0.019</b>	<b>0.105 <math>\pm</math> 0.033</b>	0.136 $\pm$ 0.049	
+Ours (DMA)	<b>0.591 <math>\pm</math> 0.028</b>	<b>0.546 <math>\pm</math> 0.017</b>	<b>0.497 <math>\pm</math> 0.060</b>	0.133 $\pm$ 0.029	0.094 $\pm$ 0.036	0.125 $\pm$ 0.045	

Table 9. Mean  $\pm$  std. err. of the Mutual-Information Gap (MIG) scores of four post-hoc methods applied to the embedding spaces of four disentanglement models on two datasets with different pairs of correlated variables. The MIG is computed across all components of the dataset.

to be smoothed or aggregated by some technique such as IG or SG. Figure 16 illustrates the correlation between the ground-truth attribute representation (scores) and predicted representation by using our model (using plain gradients) for the top discovered component. The two components are clearly correlated, but more in a block-sense: Classes with low scores on the attribute received low scores on the discovered component. The same holds for high scores, but within these, we observe stronger noise, which explains why the Spearman’s correlation values were imperfect. This can be due to a certain degree of arbitrage in the ground-truth attribute values of each class. Here, Fig. 17, just like Fig. 6 in the main paper, shows qualitative examples, including the ground-truth values which appear to fluctuate. We emphasize that this analysis should be viewed as a take on quantifying the quality of interpretable components, but that a refined benchmark is material for future work.

Dataset		Shapes3D			MPI3D-real		
Correlated factors	floor vs. background	orientation vs. background	orientation vs. size	background vs. object color	background vs. robot arm dof-1	robot arm dof-1 vs. robot arm dof-2	
<b>BetaVAE</b>	<b>0.834 ± 0.022</b>	<b>0.839 ± 0.053</b>	0.828 ± 0.011	0.557 ± 0.032	0.490 ± 0.044	0.412 ± 0.022	
	+PCA	0.722 ± 0.060	0.689 ± 0.047	0.393 ± 0.037	0.452 ± 0.031	0.398 ± 0.031	
	+ICA	0.797 ± 0.036	0.775 ± 0.083	0.385 ± 0.100	0.262 ± 0.061	0.251 ± 0.031	
	+Ours (IMA)	0.767 ± 0.108	0.808 ± 0.060	<b>0.832 ± 0.022</b>	0.565 ± 0.022	0.504 ± 0.036	0.443 ± 0.027
	+Ours (DMA)	0.813 ± 0.087	0.829 ± 0.068	0.826 ± 0.029	<b>0.567 ± 0.024</b>	<b>0.525 ± 0.042</b>	<b>0.444 ± 0.027</b>
<b>FactorVAE</b>	0.636 ± 0.045	0.622 ± 0.064	0.595 ± 0.050	<b>0.354 ± 0.016</b>	<b>0.389 ± 0.015</b>	0.342 ± 0.006	
	+PCA	0.627 ± 0.071	<b>0.680 ± 0.027</b>	<b>0.652 ± 0.024</b>	0.330 ± 0.018	0.388 ± 0.022	<b>0.353 ± 0.016</b>
	+ICA	0.619 ± 0.059	0.446 ± 0.146	0.200 ± 0.148	0.277 ± 0.013	0.242 ± 0.082	0.304 ± 0.017
	+Ours (IMA)	<b>0.663 ± 0.022</b>	0.661 ± 0.028	0.644 ± 0.051	0.347 ± 0.007	0.386 ± 0.020	0.337 ± 0.013
	+Ours (DMA)	0.646 ± 0.026	0.637 ± 0.023	0.619 ± 0.026	0.330 ± 0.015	0.375 ± 0.016	0.335 ± 0.013
<b>BetaTCVAE</b>	0.676 ± 0.012	0.814 ± 0.052	0.877 ± 0.015	0.445 ± 0.044	0.379 ± 0.021	0.346 ± 0.020	
	+PCA	0.761 ± 0.035	0.738 ± 0.063	0.794 ± 0.037	<b>0.505 ± 0.040</b>	<b>0.425 ± 0.012</b>	0.389 ± 0.008
	+ICA	0.834 ± 0.004	0.761 ± 0.051	0.806 ± 0.051	0.149 ± 0.099	0.168 ± 0.053	0.057 ± 0.035
	+Ours (IMA)	0.837 ± 0.004	0.849 ± 0.015	<b>0.879 ± 0.013</b>	0.463 ± 0.048	0.401 ± 0.018	0.399 ± 0.019
	+Ours (DMA)	<b>0.842 ± 0.000</b>	<b>0.854 ± 0.017</b>	0.878 ± 0.013	0.460 ± 0.046	0.399 ± 0.018	<b>0.399 ± 0.014</b>
<b>DipVAE</b>	<b>0.826 ± 0.006</b>	0.839 ± 0.006	0.785 ± 0.033	<b>0.517 ± 0.046</b>	<b>0.473 ± 0.046</b>	0.430 ± 0.013	
	+PCA	0.671 ± 0.019	0.603 ± 0.064	0.653 ± 0.039	0.431 ± 0.028	0.373 ± 0.027	0.344 ± 0.021
	+ICA	0.826 ± 0.006	0.831 ± 0.007	0.749 ± 0.027	0.434 ± 0.042	0.423 ± 0.027	0.424 ± 0.012
	+Ours (IMA)	0.824 ± 0.007	0.812 ± 0.018	0.785 ± 0.029	0.503 ± 0.044	0.471 ± 0.035	0.436 ± 0.021
	+Ours (DMA)	0.822 ± 0.006	<b>0.850 ± 0.012</b>	<b>0.809 ± 0.045</b>	0.505 ± 0.040	0.459 ± 0.040	<b>0.448 ± 0.026</b>

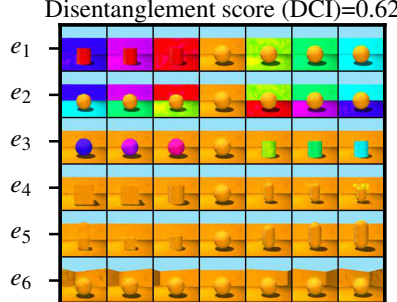
Table 10. Mean ± std. err. of the FactorVAE scores of four post-hoc methods applied to the embedding spaces of four disentanglement models on two datasets with different pairs of correlated variables. The FactorVAE score is computed across all components of the dataset.

Dataset		Shapes3D			MPI3D-real		
Correlated factors	floor vs. background	orientation vs. background	orientation vs. size	background vs. object color	background vs. robot arm dof-1	robot arm dof-1 vs. robot arm dof-2	
<b>BetaVAE</b>	0.086 ± 0.003	0.119 ± 0.004	0.100 ± 0.005	0.127 ± 0.014	0.098 ± 0.015	<b>0.092 ± 0.025</b>	
+PCA	0.047 ± 0.005	0.062 ± 0.006	0.066 ± 0.006	0.027 ± 0.005	0.055 ± 0.008	0.037 ± 0.006	
+ICA	0.007 ± 0.001	0.013 ± 0.001	0.019 ± 0.004	0.017 ± 0.006	0.007 ± 0.002	0.004 ± 0.001	
+Ours (IMA)	<b>0.099 ± 0.026</b>	0.114 ± 0.008	0.112 ± 0.007	<b>0.131 ± 0.011</b>	<b>0.113 ± 0.005</b>	0.082 ± 0.024	
+Ours (DMA)	0.094 ± 0.020	<b>0.127 ± 0.012</b>	<b>0.114 ± 0.013</b>	0.107 ± 0.025	0.059 ± 0.024	0.037 ± 0.013	
<b>FactorVAE</b>	0.072 ± 0.006	0.059 ± 0.006	<b>0.064 ± 0.001</b>	0.059 ± 0.004	0.066 ± 0.008	0.054 ± 0.003	
+PCA	0.060 ± 0.006	<b>0.066 ± 0.004</b>	0.057 ± 0.004	<b>0.065 ± 0.008</b>	<b>0.076 ± 0.004</b>	<b>0.071 ± 0.003</b>	
+ICA	0.013 ± 0.002	0.008 ± 0.001	0.006 ± 0.002	0.002 ± 0.000	0.002 ± 0.001	0.001 ± 0.000	
+Ours (IMA)	<b>0.077 ± 0.012</b>	0.052 ± 0.005	0.054 ± 0.017	0.054 ± 0.006	0.059 ± 0.006	<b>0.036 ± 0.015</b>	
+Ours (DMA)	0.071 ± 0.014	0.053 ± 0.012	0.040 ± 0.010	0.041 ± 0.017	0.043 ± 0.015	0.044 ± 0.013	
<b>BetaTCVAE</b>	0.052 ± 0.002	0.107 ± 0.013	0.096 ± 0.016	<b>0.151 ± 0.017</b>	<b>0.133 ± 0.007</b>	<b>0.117 ± 0.011</b>	
+PCA	0.073 ± 0.004	0.075 ± 0.011	0.107 ± 0.015	0.148 ± 0.018	0.125 ± 0.009	0.109 ± 0.007	
+ICA	0.015 ± 0.000	0.010 ± 0.001	0.011 ± 0.002	0.011 ± 0.004	0.005 ± 0.002	0.004 ± 0.002	
+Ours (IMA)	0.105 ± 0.003	0.119 ± 0.012	<b>0.130 ± 0.023</b>	0.055 ± 0.017	0.059 ± 0.016	0.056 ± 0.003	
+Ours (DMA)	<b>0.108 ± 0.005</b>	<b>0.127 ± 0.013</b>	0.109 ± 0.017	0.071 ± 0.020	0.072 ± 0.010	0.051 ± 0.015	
<b>DipVAE</b>	0.083 ± 0.004	0.084 ± 0.003	0.070 ± 0.002	0.056 ± 0.011	0.039 ± 0.013	0.057 ± 0.016	
+PCA	0.027 ± 0.003	0.034 ± 0.006	0.043 ± 0.004	0.023 ± 0.004	0.030 ± 0.008	0.022 ± 0.005	
+ICA	0.006 ± 0.001	0.003 ± 0.002	0.030 ± 0.002	0.011 ± 0.005	0.005 ± 0.003	0.005 ± 0.002	
+Ours (IMA)	0.089 ± 0.012	0.082 ± 0.005	0.077 ± 0.002	<b>0.060 ± 0.008</b>	<b>0.047 ± 0.010</b>	<b>0.061 ± 0.016</b>	
+Ours (DMA)	<b>0.114 ± 0.003</b>	<b>0.105 ± 0.008</b>	<b>0.084 ± 0.007</b>	0.051 ± 0.008	0.043 ± 0.012	0.054 ± 0.016	

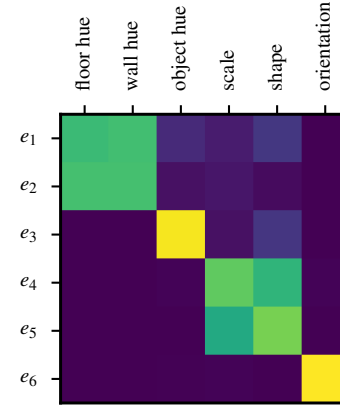
Table 11. Mean ± std. err. of the SAP scores of four post-hoc methods applied to the embedding spaces of four disentanglement models on two datasets with different pairs of correlated variables. The SAP score is computed across all components of the dataset.

Num. components	K=1	K=10	K=20	K=30	K=40	K=50	K= 60
Baseline (random)	0.659 ± 0.017	0.618 ± 0.012	0.585 ± 0.011	0.559 ± 0.011	0.536 ± 0.010	0.516 ± 0.009	0.492 ± 0.010
PCA	<b>0.789 ± 0.024</b>	0.602 ± 0.007	0.497 ± 0.005	0.440 ± 0.006	0.402 ± 0.004	0.372 ± 0.004	0.346 ± 0.004
ICA	0.515 ± 0.028	0.442 ± 0.005	0.412 ± 0.006	0.390 ± 0.007	0.370 ± 0.007	0.353 ± 0.007	0.335 ± 0.006
Ours-IMA,Grad	0.657 ± 0.025	0.601 ± 0.009	0.564 ± 0.009	0.535 ± 0.008	0.510 ± 0.009	0.488 ± 0.010	0.463 ± 0.012
Ours-IMA,IG	0.705 ± 0.044	0.613 ± 0.015	0.569 ± 0.012	0.541 ± 0.011	0.517 ± 0.010	0.493 ± 0.008	0.468 ± 0.006
Ours-IMA,SG	0.653 ± 0.026	0.599 ± 0.010	0.563 ± 0.007	0.553 ± 0.015	0.534 ± 0.014	0.515 ± 0.015	0.469 ± 0.007
Ours-DMA,Grad	0.701 ± 0.045	0.626 ± 0.029	0.585 ± 0.028	0.559 ± 0.011	0.535 ± 0.029	0.515 ± 0.030	0.490 ± 0.030
Ours-DMA,IG	0.710 ± 0.020	<b>0.657 ± 0.008</b>	<b>0.615 ± 0.013</b>	<b>0.587 ± 0.016</b>	<b>0.562 ± 0.018</b>	0.539 ± 0.021	0.514 ± 0.021
Ours-DMA,SG	0.686 ± 0.020	0.641 ± 0.031	0.610 ± 0.032	0.584 ± 0.032	0.561 ± 0.033	<b>0.540 ± 0.033</b>	<b>0.516 ± 0.033</b>

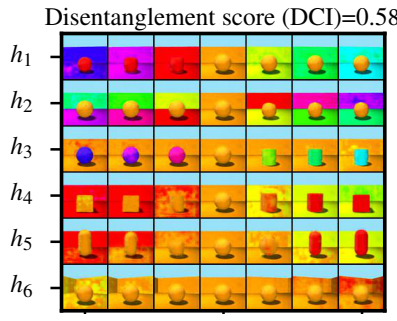
Table 12. Quantitative comparison of discovered components using our methods, PCA, ICA and a random baseline. Mean correlation score of top-K (K in column) discovered components are shown in (mean ± std.) for five runs.



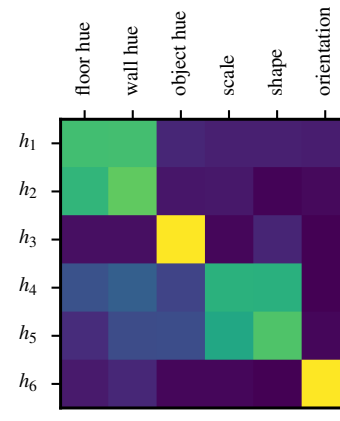
(a) BetaTCVAE



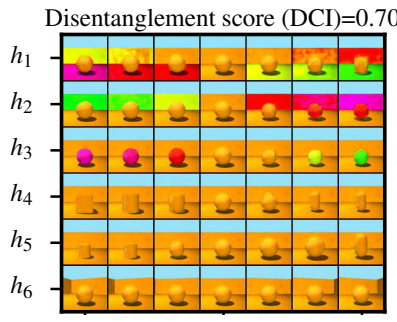
(b) Corresponding linear entanglement matrix



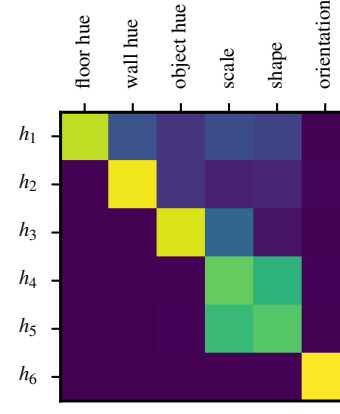
(c) BetaTCVAE + ICA



(d) Corresponding linear entanglement matrix



(e) BetaTCVAE + Ours (DMA, SG)



(f) Corresponding linear entanglement matrix

Figure 15. Traversal plots from another model (BetaTCVAE) trained on the correlated dataset. As for all traversal plots in this paper, we manually permuted the dimensions to match across plots. In addition, we compute a matrix of linear entanglement that shows which ground truth factors are changed when moving into a certain direction (brightness corresponds to magnitude of change). While none of the post-hoc methods manages to disentangle shape and size (most likely due to their non-linear encoding), our model resolves the linearly entangled factors *floor hue* and *wall hue* fairly well, which can also be seen from the entanglement matrix.

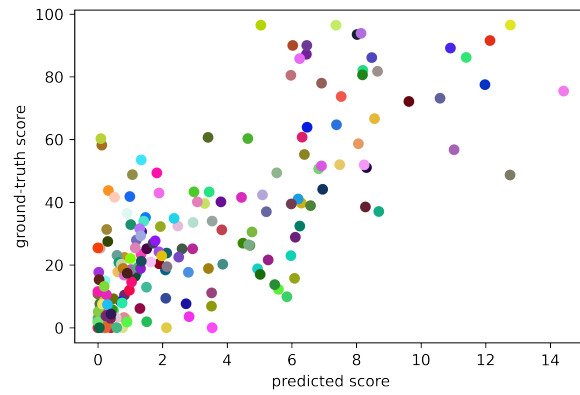


Figure 16. Correlation between ground-truth attribute scores and our predicted scores for the best matched component. Each dot represents a class.

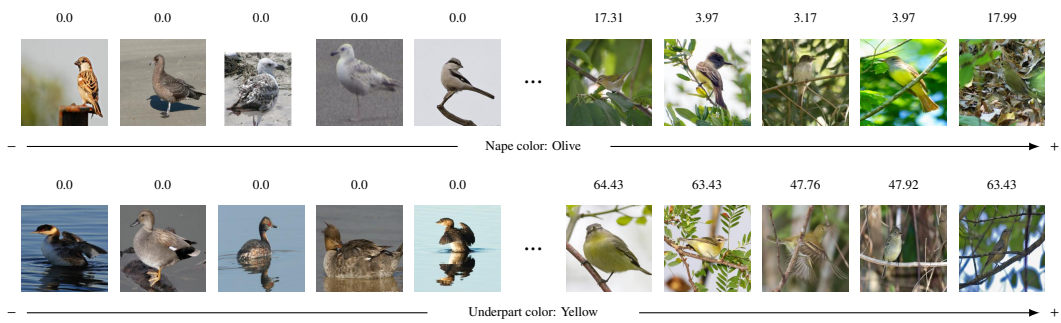


Figure 17. Examples of discovered components on CUB. The corresponding ground-truth attribute is shown under images and the ground-truth value of each image is depicted above the image. “+/-” indicate the positive/negative direction along the discovered concept.